

1 POSTGLACIAL DEFORMATION HISTORY OF SACKUNGEN ON THE NORTHERN SLOPE
2 OF PIC D'ENCAMPADANA, ANDORRA (manuscript v.4; 08-JAN-2019)

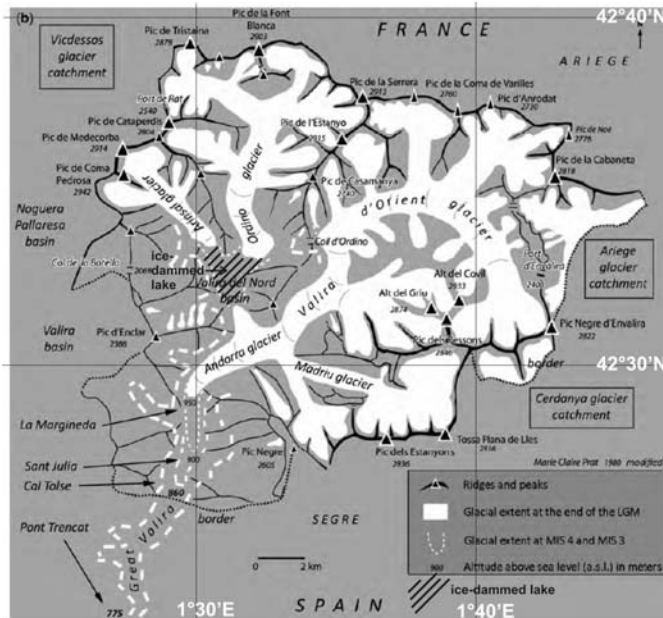
3
4 J.P. McCalpin, J. Corominas
5

6
7 **ABSTRACT**

8 The northern slope of Pic d'Encampadana descends steeply 800 m down into the glaciated
9 Valira d'Orient Valley of Andorra, in the eastern Pyrenees. This high, steep slope is underlain by
10 foliated metamorphic rocks (slates, phyllites) and has long been known for its numerous
11 antislope scarps (sackungen), indicative of deep-seated gravitational slope deformation
12 (DSGSD). We excavated trenches across antislope scarps and their adjacent troughs at three
13 locations, to expose the trough stratigraphy, to map and date the deformation structures, and to
14 infer slope kinematics at each location. Sackung troughs formed at Encampadana have acted
15 as sediment traps since formation, and are underlain by distinctive post-faulting strata that
16 permit reconstructing the evolution of the scarp/trough pair. The oldest strata exposed in our 2-
17 2.5 m-deep trenches are coarse, angular talus deposited as slope-mantling sediments predating
18 the modern narrow sackung scarps and troughs. These deposits have been disrupted by normal
19 and reverse faulting, with the largest fault zone underlying the antislope scarp and dipping into
20 the slope at 40°-80°. Each trench contains subsidiary north-dipping normal faults beneath the
21 southern edge of the trough, giving the appearance of a graben. In two of three trenches post-
22 faulting deposits have subsequently been tilted or folded down toward the main fault, as if
23 sagging into a void space created by horizontal extension and/or outward toppling of the
24 footwall. The trough fill is generally dominated by poorly-sorted sandy slopewash, but does
25 contain two other important facies: (1) thin clay and silt deposits deposited in standing water,
26 found beneath the center of the trough, and (2) gravelly scarp-derived colluvial wedges, found
27 beneath the edges of the trough. Paleosols have formed on the top of fining-upward sequences
28 of strata, permitting interpretation of several cycles of: (1) episodic downdropping along graben
29 faults and deepening of the topographic trough, (2) filling the trough with marginal colluvial and
30 axial sag-pond sediments, followed by (3) a hiatus of soil profile development. Despite their
31 shallow depths, each trench preserves evidence of multiple unconformities and 3 to 5
32 deformation events, recognized by: (1) upward termination of faults at various stratigraphic
33 levels; (2) angular unconformities between trough infill units or fining-upward packages; and (3)
34 by coarse, angular colluvial deposits that thin away from the footwall (scarp-derived colluvial
35 wedges). The average time between deformation events in any one trench in the past 12-15 ka
36 is about 3-3.5 ka. Deformation seems to have begun first in the lower part of the northern slope
37 (Trench 2, 1935 m elevation) about 15.3 ka, and had spread to the upper parts of the slope
38 (Trench 3, 2320 m) by 11.6 ka. Deformation in the lower slope ceased after 5.5 ka, but still
39 continued higher on the slope into the mid-late Holocene. The youngest deformation dated (1.4-
40 1.6 ka) occurred in the highest trench on the slope. This pattern of younger deformation with
41 increasing elevation has been documented at several other sites (e.g., Panek and Klimes, 2016)
42 and has been ascribed to an upslope-migrating extensional stress field which originated at the
43 base of the slope from glacial oversteepening and end-glacial debuttressing.
44

45 **1. Introduction**

46 The formerly glaciated valleys of Andorra, like valleys elsewhere in the Pyrenees, display
47 abundant landforms attesting to post-glacial rock slope failure (Jarman et al., 2014). In the
48 Valira d'Orient (Fig. 1) a large trunk glacier has eroded a U-shaped valley in multiple
49 Pleistocene glaciations to a depth of 600 m below the global Late Glacial Maximum (LGM)
50 trimline. The valley walls in central Andorra are composed of relatively weak, foliated Paleozoic
51 slates and phyllites, similar to those studied by Zischinsky (1966) in his classic early paper
52 about sackungen.
53



54
55 Fig. 1. Late Pleistocene ice extent at the end of the global Late Glacial Maximum (LGM) in Andorra, in
56 relation to the Encampadana study area (box at center; also the area of Figs. 4 and 6). Canillo village is
57 located at the NW corner of the box. Adapted from Turu et al, 2016.

58
59 This combination of deep valleys, steep valley sidewalls, weak foliated rocks, and moderate
60 precipitation (1100 mm/yr in Canillo village) has spawned a wide spectrum of postglacial slope
61 failures, including (in order of increasing size) slumps, earthflows, rockslides, and deep-seated
62 gravitational slope deformation (DSGSD). This study focuses on the well-known DSGSD
63 landforms on the northern slope of Pic d'Encampadana, which lies directly west of the
64 GrandValira – Soldeu ski resort (Fig. 2).
65



66
67 Figure 2. Overall view of the northern slope of the Encampadana massif (center) looking East, with Pic
68 d'Encampadana (2472 m) at upper right and the Valira d'Orient (1561 m) at lower left. The steep forested
69 slope at center contains the studied sequence of approximately 10 antislope scarps (which can be seen
70 as small nicks in the skyline profile) and our three trench sites.

71
72

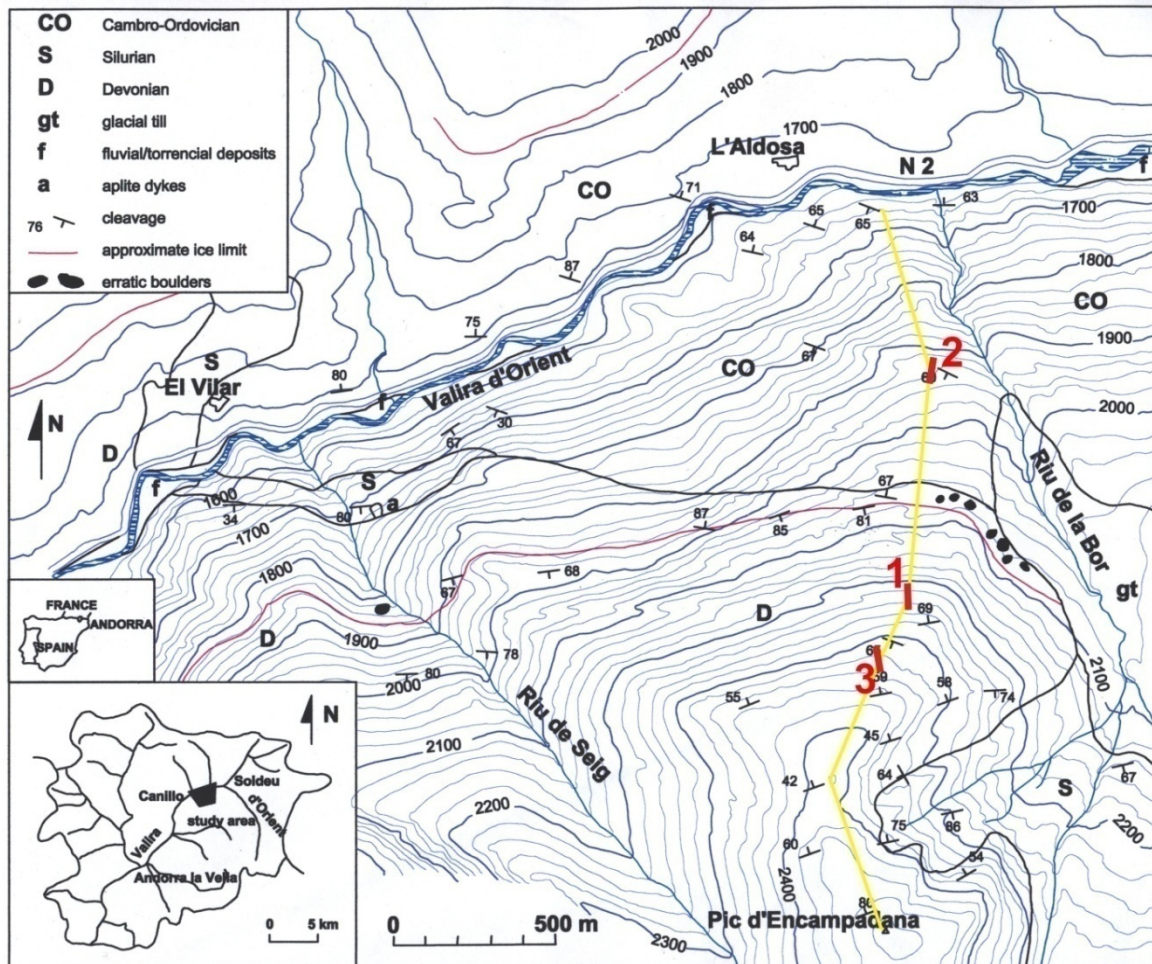
73 2. Geological Setting

74 Geologically the Encampadana massif is located in the Central-Eastern part of the Pyrenean
75 Axial Zone. The geology of the Central Pyrenees was described by Hartevelt (1970), Zwart
76 (1979), and Barnolas and Chiron (1996). The massif belongs to the synclinorium of Tort-
77 Casamanya which is arranged in a E-W direction. The bedrock of the study area is composed of
78 rocks of Paleozoic age (Silurian to Mid Devonian). An updated summary of the composition and
79 stratigraphy of the geological formations outcropping in the massif is provided by Clariana
80 (2004) and references therein.

81 The stratigraphical succession in the Encampadana massif includes the following materials:

82 (i) Cambro-Ordovician rocks, which outcrop in the Northern part of the slope (Fig. 3). They
83 consist of dark coloured phyllites, quartz-phyllites and light coloured quartzite layers with
84 thicknesses ranging from a few millimetres to a few metres. They are assigned to the Seo
85 formation (Hartevelt, 1970)

86 (ii) Silurian rocks, (Hartevelt, 1970) which are mainly composed of black carbonaceous shales
87 and of an alternation of black limestones and shales in the upper part. The Silurian rocks are
88 intensely foliated and folded. The unit has variable thickness because it is often the decollement
89 level of the Pyrenean thrusts and this causes shearing and squeezing of the beds. Locally this
90 unit forms diapiric structures of incompetent behaviour (Zwart, 1979). Silurian rocks appear
91 strongly weathered in outcrop. They are characterized by rusty brown yellow and white colors
92 due to oxidation of pyrite and subsequent sulphur precipitation.
93



95
96 Fig. 3. Geologic map of the northern slope; contour interval 20 m. Yellow line shows line of topographic
97 profile in Fig. 4. Trenches 1, 2, and 3 in red.
98
99

100 (iii) The Devonian series range from lutites and calcareous lutites interbedded with thin
101 limestones layers (Rueda formation) to massive (up to 60m thick) limestones and marly
102 limestones (Castanesa Formation), and to green to beige marly limestones (Manyanet
103 formation). All these materials have undergone long and complex deformation processes, due
104 to the superposition of the Alpine orogeny over the previous Variscan phase of deformation.
105

106 From a structural point of view, pre-Carboniferous rock formations strike E-W or ENE-WSW.
107 They define antiformal and synformal domes of kilometeric extent, bounded by faults and thrusts
108 with the same orientation. The Encampadana massif is mostly composed of Devonian rocks
109 overlaying the Silurian shales. The latter outcrop at the Collet de les Solanelles and farther East.
110

111 112 **Glaciation of Andorra and the Valira d'Orient**

113 Within the past decade the chronology of Pleistocene glaciation in the Pyrenees has been
114 significantly revised based on new suites of numerical ages from: (1) glacial landforms obtained
115 with in situ-generated cosmogenic radionuclide (CRN); (2) glacio-fluvial outwash sediments
116 obtained with optically stimulated luminescence (OSL); and (3) from the cross-correlation of

117 these dates with the radiocarbon ages of the ice-marginal deposits (Calvet et al. 2011). The
118 largest remaining data gap is uncertainty on the extent of pre-Würmian glaciers. During the
119 Würmian maximum ice extent W(MIE), glaciers often buried, eroded or reworked the terminal
120 deposits of earlier glaciations, thus hiding their evidence in today's landscape. An updated
121 review of history of the glaciations in the Pyrenees can be found at Calvet et al. (2011), Delmas,
122 (2015), and in the references therein.

123
124 During the Last Glacial cycle in the Pyrenees, glaciers occupied much of the territory. On the
125 southern side of the range glaciers were confined within the Pyrenean valleys and reached
126 lengths of 20-30 kilometers, with the fronts located between 800-1000 meters elevation (Calvet,
127 2004). According to Delmas (2015), the WMIE in the Pyrenees occurred during MIS 4 (74 – 60
128 ka). This and other recent studies (Calvet et al. 2011; García-Ruiz et al. 2013; Turu et al. 2016)
129 conclude that several episodes of high magnitude glacier advance and retreat existed after MIS
130 4. However, the number and extent of such fluctuations is still subjected to debate. Furthermore,
131 recent dating in several Pyrenean valleys has shown a contrasting behavior of glaciers.
132 Depending on the valley, glaciers reached their respective WMIE at different times, often long
133 before the global Last Glacial Maximum (LGM) (Calvet et al., 2011; Delmas et al., 2011;
134 Delmas, 2015).

135
136 Subsequent to the WMIE, Pyrenean glaciers retreated significantly in some valleys (Delmas et
137 al 2011). A major readvance took place around 23-19 ky BP, synchronous with the LGM
138 although it was less extensive than the WMIE (García-Ruiz et al. 2003, 2010; Delmas, 2015).
139 Soon after the LGM the Pyrenean ice margin went into a major and rapid recession. Even
140 before the beginning of the Late-glacial, the main trunk glaciers had already retreated to the
141 upper part of the valleys. After the Oldest Dryas (13.35-13.48ka) the glacier fronts were
142 confined to the cirques (Turu, 2011). During the Younger Dryas (11.56-12.7 ka) glaciers were
143 only capable of reaching the valley bottom and after 10 ka they were confined to the highest
144 cirques (Copons and Bordonau, 1994).

145
146 In the Principality of Andorra, the Valira d'Orient glacier had a larger accumulation zone than
147 that of the Valira del Nord and due to its orientation it was relatively sheltered from ablation
148 (Turu et al. 2015). These factors allowed the Valira d'Orient glacier to intermittently dam the pro-
149 glacial streams of the receding Valira del Nord glacier at the cuvette of Andorra la Vella (figure
150 1). This situation generated an ice-dammed lake in La Massana, the sediments of which have
151 provided the chronostratigraphic clues for reconstructing the Würmian glacial evolution in
152 Andorra (Turu et al. 2016). The retreat after the WMIE disconnected the glacier of the North
153 Valira from the Great Valira glacier. The former receded upstream of La Massana while the
154 Valira d'Orient receded upstream of Canillo. During the LGM the glacier of the Great Valira
155 reached again Andorra la Vella and was large enough to obstruct again the Valira del Nord
156 Valley. According to Turu et al. (2016), the disconnection of the two glaciers and the formation
157 of the lake took place before 25.64 ± 0.19 ka BP (19,352 to 30,482 cal BP).

158
159 During the WMIE, ice-marginal deposits accumulated on the right bank of the Valirad'Orient
160 river above the village of Canillo, at the Bordes de Montaup, and Bordes de Mereig
161 (Soutadé,1988). The deposits are located approximately 300 meters above the current valley
162 bottom, which indicates the approximate thickness of the glacier as itflowed by the
163 Encampadana massif.

164
165 **Landslides and DSGSDs in the Central & Eastern Pyrenees**
166 Slope failures in the axial Pyrenees are controlled by three mainfeatures (Corominas and
167 Baeza, 1992): (i) The presence of susceptible lithologies. Widespread shallow failures in the

168 form of shallow slides and debris flows are associated with unconsolidated deposits of glacial
169 and periglacial origin (e.g. till, glacio-lacustrine deposits, colluvium) although the large rock
170 slope deformations and failures involve weak geological units such as the Silurian shales. A
171 synthesis of the most susceptible ones is included in Corominas (1989). (ii) The erosive action
172 of the Pleistocene glaciers and the incision of the present fluvial network, locally exacerbated by
173 the orogenic uplift, have resulted in a steep relief, which constitutes the main predisposing factor
174 for instability; (iii) The geological structure plays a fundamental role in failures that require the
175 contribution of the planes of weakness such as the deep seated gravitational slope
176 deformations (DSGDD). Main fold axes and thrust fronts follow an East-West orientation. River
177 valleys running parallel to these geological structures display large slope failures as observed in
178 some central Pyrenean valleys (Soeters and Rengers, 1983; Bordonau and Vilaplana, 1986) as
179 well as most of the Andorran valleys (Jarman et al. 2014)

180

181 **3. Methods**

182 *Trenching:* We excavated three trenches with picks and shovels across sacking troughs near
183 the toe, midslope, and head of the northern slope. Trenches were roughly 60 cm wide, 4.5-6 m
184 long, and 2-2.5 m deep. The eastern wall of each trench was cleaned and gridded with string,
185 after which we drew a field trench log on graph paper at a scale of 1:15. Those logs were then
186 digitized for this paper. Unconsolidated stratigraphic units were defined based on color, texture,
187 and sedimentary structures. Soil horizons developed on deposits (parent materials) were also
188 identified and labelled according to the A/B/C horizon terminology used in the USA (e.g., Soil
189 Survey Staff, 2014).

190

191 *Geochronology:* Our three trenches were sited in parts of sacking troughs that were closed (or
192 nearly closed) topographic depressions, in hopes that trough sediments would contain organics
193 (amenable to radiocarbon dating) or fine-grained deposits (amenable to luminescence dating).
194 Each trench contained both datable organics and silty sediments. Radiocarbon samples were
195 detrital charcoal or in-situ burn layers, dated by AMS. We used the calibration curve of Reimer
196 et al. (2013) to convert radiocarbon years to calendar years. Fine-grained sediments were dated
197 by the infrared-stimulated luminescence (IRSL) method. The multi-aliquot IRSL method was
198 employed by Glenn Berger at the Desert Research Institute, Reno, Nevada. The polymineralic,
199 non-carbonate, detrital 4-11 μm diameter size fraction was prepared. Laboratory sample-
200 preparation procedures have been outlined elsewhere (e.g., Berger, 1990; Wintle and Huntley,
201 1980). U and Th concentrations were measured by the thick-source-alpha-particle counting
202 (TSAC) technique (Huntley and Wintle, 1981) on dried powders. K was measured by
203 commercial atomic absorption spectrophotometry. Radioactive secular equilibrium is assumed,
204 and assumption apparently valid for luminescence dating of many sediments but not of all
205 alluvial sediments (Olley et al., 1996). The basic sealed-chamber TSAC test (Huntley and
206 Wintle, 1981) indicates no significant radon loss from the dried sample powders used in the
207 study, except for sample OSL3-3, for which an increase-on-sealing of $14\pm 4\%$ in the total TSAC
208 count rate was observed. This increase could indicate that significant radon loss has occurred
209 and is occurring within sediments surrounding this sample.

210

211 For IRSL measurements the deep-blue luminescence near the known 410-nm emission from
212 the most K-rich feldspars was chosen for detection (e.g. Aitken, 1998). To convert the sample's
213 fossil light to an absorbed-energy equivalent, calibrated laboratory beta (^{90}Sr - ^{90}Y) and alpha
214 (^{241}Am) sources were used. Signal was recorded with an automated, high-capacity Daybreak
215 Nuclear Model 1150 reader using an EMI 9635Q photomultiplier tube. Dose-response curves
216 and other data were processed with software produced by Glenn Berger (e.g., Berger et al,
217 1987).

218

219 **4. Results**

220

221 **4.1. Geology and Geomorphology of the Northern Slope**

222 The trimline of the Latest Glacial Maximum (LGM) Valira d'Orient glacier crosses the northern
223 slope from about 2100 m on the upvalley (east) side, to 1850 m on the downvalley side (thin red
224 line on Fig. 3). The trimline is marked by the sudden appearance of rounded erratic boulders of
225 granitic composition, which contrast to the angular, locally-derived clasts of dark Lower
226 Paleozoic phyllite and slate.

227

228 The most abundant geomorphic expressions of DSGSD on the northern slope are contour-
229 parallel antislope scarps found from low on the slope to its head at the Solanelles Graben (Fig.
230 4). Such small scarps have also been referred to in the literature as counter-slope scarps,
231 counterscarps, and uphill-facing scarps. Hurliman et al. (2016) described the slope as follows:
232 *“The field data at Encampadana show the typical morphological features of a DSGSD such as a*
233 *prominent graben at the top of the slope and many large counterscarps. The structural data*
234 *measured in the area indicated two important discontinuity sets: a subvertical schistosity parallel*
235 *to the valley axis [our Fig. 4], which favored the general toppling of large slope-parallel blocks,*
236 *and a subvertical perpendicularly orientated joint system, which divided these rock blocks.”*

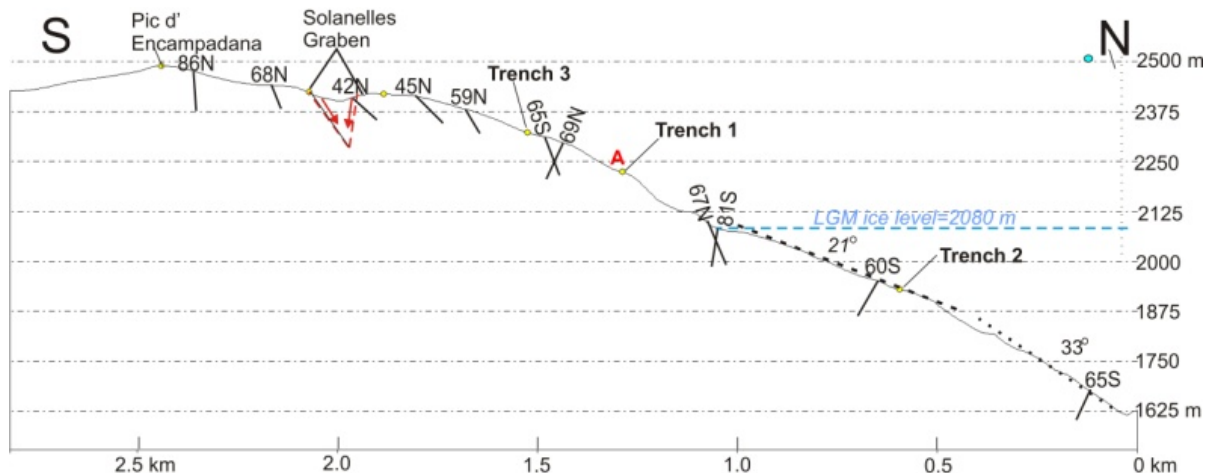
237

238 Most scarps on the slope are short (200-400 m), trend east-west, and have a swarm-like pattern
239 in map view. Their east-west strike is about 15° oblique (clockwise) to the SW-NE-trending
240 topographic contours. Scarp orientation is thus similar to the strike of foliation/cleavage in the
241 metamorphic bedrock. The longest antislope scarp zone is 1500 m long and lies on the steepest
242 part of the entire slope, about 120 m above the LGM ice limit (Fig. 5). It consists of three
243 abnormally high antislope scarps each about 500 m long, which form a left-stepping pattern and
244 descend obliquely across the slope from ~2200 m elevation at the east end to 2000 m at the
245 west end. Assuming that the scarps represent displacement on extensional (normal faults), the
246 left-stepping pattern implies a left-oblique sense of displacement (Crider, 2001).

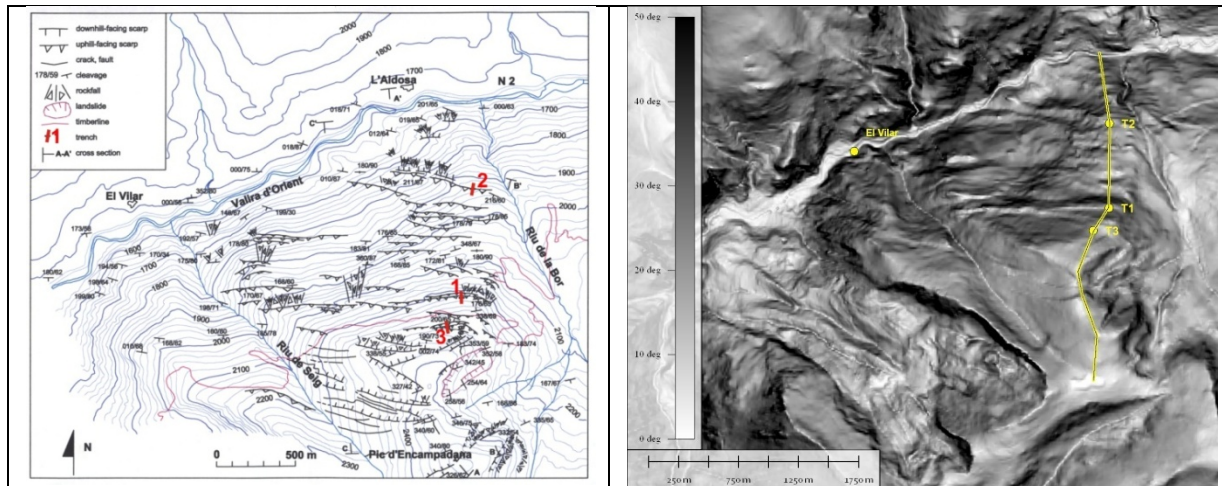
247

248

249



250 Fig. 4. Topographic profile of the northern slope through our three trench sites (line of section shown in
251 yellow on Figs. 3, 5b). Small black lines with numbers are dip angles of the dominant foliation/cleavage in
252 bedrock. Strike is approximately perpendicular to the section. Red “A” marks the longest (1.5 km) and
253 highest scarp zone.
254



255 Fig. 5. Maps of slope deformation landforms on the north slope of Pic d'Encampadana. (a) Left, antislope
 256 scarps and other landforms related to deep-seated and shallow gravitational deformation. Trench sites
 257 are shown in red. Contour interval 20 m. (b) Right, slopeshade image made from a 5 m lidar DEM
 258 (Spanish National Inst. of Geography). Prominent east-west bands on Encampadana's lower slopes are
 259 antislope scarps and benches (light) and downhill-facing scarps (dark) created by toppling.
 260

261 4.2. Geochronology of Quaternary Deposits and Paleosols in Trenches

262 Our age control for deformation events comes from radiocarbon and IRSL dates from sediments
 263 deposited in structural depressions (Table 1). This approach to dating deformation events
 264 derives from paleoseismic studies of normal faults (e.g. McCalpin, 2009, Chapter 3). Sample
 265 locations are shown on the trench logs (Figs. 7, 9, and 12)..
 266

267 Table 1. Radiocarbon (C-14) and infrared-stimulated luminescence (IRSL) dates from the
 268 Andorra trenches (from Berger, 2000).

Trench	Unit	Material	Dating Method and Laboratory ¹	Reported Age (C14 yr BP)	Calendar Age (cal BP), 2σ ²
1	6A	soil A horizon (organic sandy loam)	AMS/NSF	1130±50	Cal AD 781 to 1003 (1014-1235 cal BP)
1	4	organic silty loam	AMS/NSF	3035±55	Cal BC 1122 to 1419 (3139-3436 cal BP)
2	10a	silt matrix of younger distal colluvium	IRSL		5.51±0.37 ka
2	5a	silt matrix of older distal colluvium	IRSL		15.3±1.1 ka
3	6g	soil A horizon (organic silty loam)	AMS/Beta	1490±40	Cal AD 442 to 499, and 518 to 643 (whole span 1374 to 1575 cal BP)
3	6a	silty younger sag pond deposit	IRSL		8.11±0.74 ka
3	3a	silty older sag pond deposit	IRSL		11.6±2.1 ka

269 ¹AMS= radiocarbon, accelerator mass spectrometry; NSF= NSF AMS Facility, Tucson, Arizona; Beta=
 270 Beta Analytic, Miami, Florida; OSL dates are infrared-stimulated luminescence dates on the 4-11 micron
 271 silt fraction from the Desert Research Institute, Reno, Nevada.

272 ² Calendar-year Calibration from CALIB Rev 7.0.4 (2017), using the IntCal13 calibration data set; see
 273 <http://calib.org> (accessed 2017-12-28) and Reimer et al., 2013. Assumes dated samples contain a 50-
 274 year average of C-14.
 275

276 IRSL dosimetry data are listed in Table 2. Ages and related luminescence data are listed in
 277 Table 3. The Th concentrations seem high, but without additional, detailed data on the spatial
 278 distribution of U and Th and without detailed isotopic data, it is necessary to assume that

279 conditions of secular equilibrium have applied throughout the samples' burial history. It is also
 280 necessary to assume that the estimated past-water-concentration values are accurate and that
 281 the measured U, Th, and K concentrations from a single sample adjacent to the IRSL sample
 282 are representative of the sediment surrounding the sample out to a radius of ~30 cm (the
 283 approximate range of ambient gamma radiation in soil). The measured present water value was
 284 used with the samples, with conservative uncertainty assigned.

285
 286 Table 2. Dosimetry data of Andorra IRSL samples.

Sample	Water ¹	K ₂ O wt.% (±0.05)	C _t ² ks ⁻¹ x cm ⁻²	C _{th} ² ks ⁻¹ x cm ⁻²	Th ppm	U ppm	b value ³ pGy x m ²	Dose rate ⁴ Gy/ka
OSL2-3	0.21±0.05	3.22	0.808±0.014	0.385±0.048	10.3±1.3	3.30±0.39	0.899±0.076	4.54±0.23
OSL2-2	0.13±0.05	2.73	0.871±0.016	0.518±0.062	13.9±1.7	2.76±0.50	0.745±0.079	4.58±0.25
OSL3-1	0.34±0.08	3.43	0.907±0.021	0.649±0.084	17.4±2.3	2.01±0.68	0.691±0.081	4.26±0.29
OSL3-3	0.34±0.08	2.65	0.864±0.017	0.544±0.064	14.6±1.7	2.50±0.52	1.08±0.27	3.98±0.34

287 ¹Estimated historic average ratio of weight of water/weight of dry sample. Uncertainties here and elsewhere are ±1σ.
 288 ²Total and thorium count rates from finely powdered samples for thick-source-alpha-particle-counting (TSAC) method
 289 [Huntley and Wintle, 1981]. C_u = C_t - C_{th}
 290 ³Alpha effectiveness factor [Huntley et al., 1988; Berger, 1988].
 291 ⁴Calculated with the conversion factors and equations given by Berger [1988] and includes a cosmic ray component
 292 of 0.15±0.03 estimated from the data of Prescott and Hutton [1988].
 293
 294

295 Table 3. IRSL data and ages for Andorra trench samples.¹

Sample	Preheat ²	D _E ³ (Gy)	Time ⁴	Age (ka)
OSL2-3	140°C/2d	25.0±1.1	1-40	5.51±0.37
OSL2-2	140°C/2d	69.8±3.5	1-40	15.3±1.1
OSL3-1	130°C/2d	34.6±2.1	1-15	8.11±0.74
OSL3-3	130°C/2d	46.1±7.2	1-40	11.6±2.1

296 ¹The polymineralic 4-11 μm size fraction was used for all IRSL measurements. IRSL was detected at the 420±20 nm
 297 spectral region (bandpass 390-470 nm at 1% cut). All bleaching was for 2 h with >780 nm solar spectrum passed..
 298 ²The chosen pre-readout heating.
 299 ³Weighted mean equivalent dose plus average error over time interval in next column. A weighted-saturating-
 300 exponential regression and error model (Berger et al., 1987) was employed for all samples.
 301 ⁴The readout (LED-on) time interval for which D_E is calculated.
 302

303 4.3. Trench 1

304 Trench 1 was located at 2230 m elevation at the eastern end of the longest antislope scarp on
 305 the northern slope (Fig. 5). Trench 1 was 4.5 m long and as much as 2.1 m deep. The trench
 306 axis was oriented N07°W, perpendicular to the sackung trough.
 307

308 *Local Geomorphology:* Trench 1 was located across an asymmetric, contour-parallel trough that
 309 occupied the southern half of a 15 m-wide bench. The deepest part of the trough lay up against
 310 a very steep slope to the south (Fig. 6, right). We trenched across the topographic low point that
 311 supported growth of lush green grass, suggesting fine-grained deposits and occasional ponding.
 312

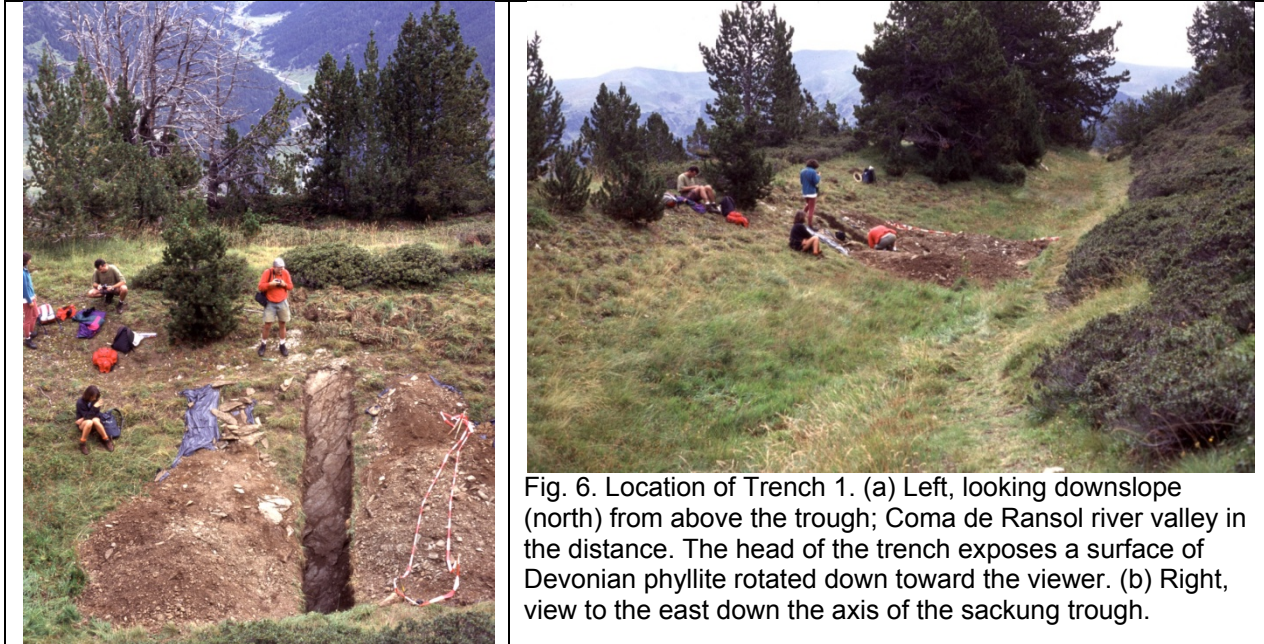


Fig. 6. Location of Trench 1. (a) Left, looking downslope (north) from above the trough; Coma de Ransol river valley in the distance. The head of the trench exposes a surface of Devonian phyllite rotated down toward the viewer. (b) Right, view to the east down the axis of the sackung trough.

313
 314
 315
 316
 317
 318
 319
 320
 321
 322
 323
 324
 325
 326
 327
 328
 329
 330
 331
 332

Stratigraphy and Soils: On the east trench wall we define 6 major units, which were further subdivided into 15 subunits (Fig. 7). Unit 1a is the intact phyllite bedrock of the downthrown block (Devonian), and units 1b and 1c are fractured and translocated counterparts of unit 1a. The oldest unconsolidated deposit (unit 2) directly overlies weathered phyllite and is composed of thin, tabular, clays (unit 2b) or clayey loams (unit 2a) that contain very weathered phyllite clasts. The strong weathering and odd (reduced) colors (green-yellow to golden yellow) suggest that unit 2 was deposited in stagnant water in a closed depression. In the deepest part of the trench (between faults F2 and F3a) unit 2 is overlain by a dark brown silty loam (unit 4). Unit 4 is interpreted as the A horizon of a buried paleosol developed on underlying unit 2. However, outside of faults F2 and F3a, there are intermediate deposits (unit 3) between units 2 and 4. North of fault F2 the intermediate unit is 3a, a gravelly sand with yellow-brown matrix. The unit coarsens toward the north and thus resembles scarp-derived colluvium; it is overlain by the unit 4 paleosol. South of fault F3a units 2 and 4 are separated by a 1.6 m-thick block of strata (unit 3) that has been tilted 30°-40° to the south and faulted (faults F3b through F3d). Based purely on color and texture, unit 3c may correlate with unit 3a in the northern part of the trench. However, that leaves the upper 1.2 m of stratigraphy in the tilted block (units 3d, 3e, 3f) with no counterparts in the rest of the trench. Unit 4 drapes the truncated edges of block stratigraphy in angular unconformity.

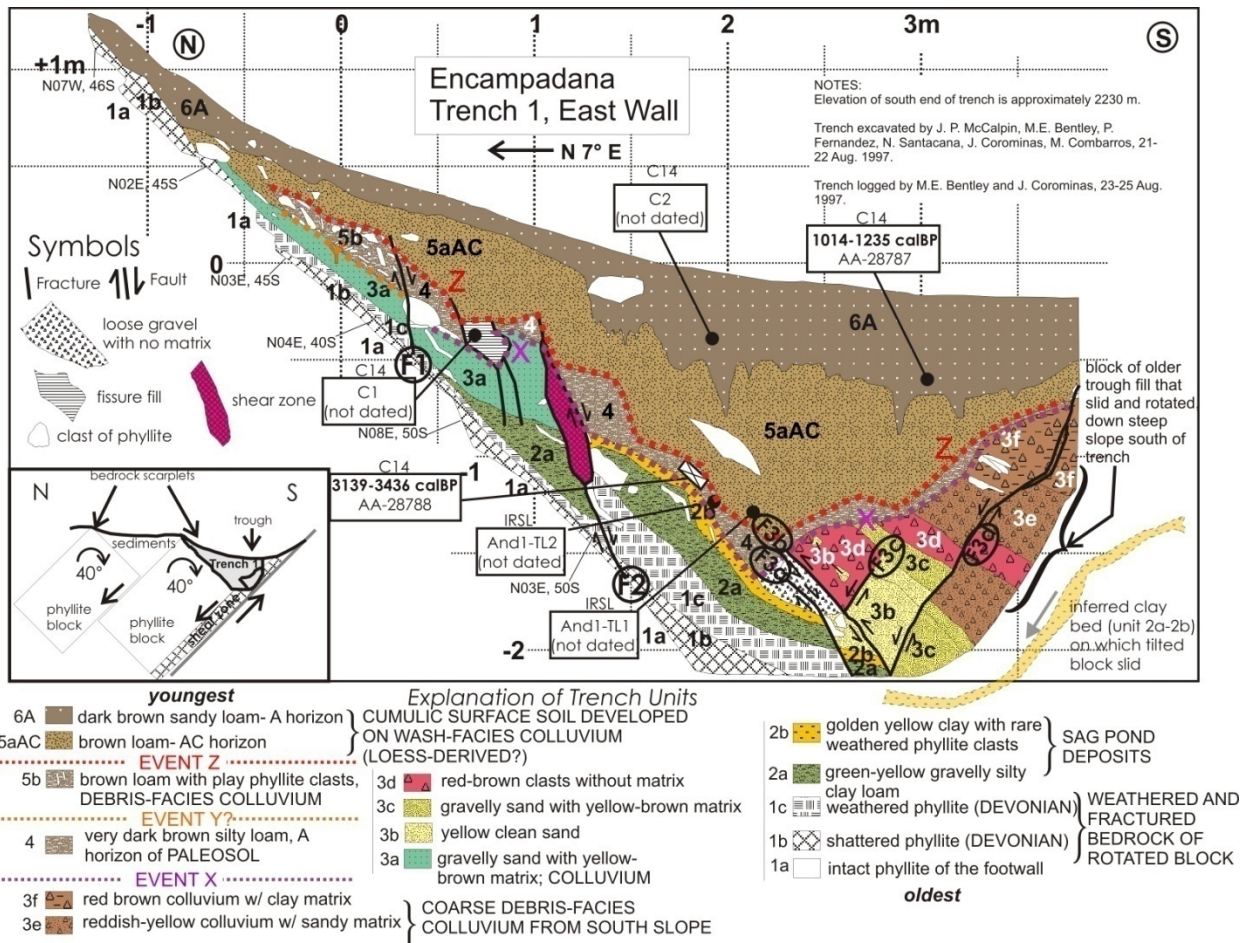


Fig. 7. Log of East Wall of Trench 1. Inset at lower left shows structures and kinematics.

Subsequent to its formation, the unit 4 paleosol has been folded into a V-shape. Atop the V are units 5a and 6, which are poorly stratified brown loam to dark brown sandy loam, respectively. Unit 5a yielded an age of 3139-3436 cal BP. We interpret units 5a and 6 as wash-facies colluvium (slopewash) that has filled in the sackung trough over long periods of time subsequent to the latest deformation event. Soil-forming processes have kept pace with trough aggradation, creating a 1.3 m-thick cumulic soil profile composed of an A horizon (unit 6A) and underlying AC horizon (unit 5aAC). North of fault F1 we identified a stone line at the base of unit 5a, which we interpret as debris-facies colluvium (unit 5b).

Structure: The northern end of the trench is composed of a smooth plane of fractured phyllite bedrock (visible in Fig. 6) which dips 40°-50°S. Faults F1 and F2 are normal faults that splay upward off this bedrock surface at steeper angles. F1 dips 80°S and displaces unit 3a about 10 cm down-to-the-south, whereas F2 dips 70°S, has a shear zone about 15 cm wide, and displaces unit 4 50 cm down-to-the-south. However, both faults have inconsistent displacement sense and/or amounts as they are traced up and down dip. For example, on F1 unit 4 exists on the south side of the fault but not on the north side. On F2 unit 4 is displaced 50 cm in a normal sense, but underlying unit 2a is displaced a smaller amount in a reverse sense (down-to-the-north). Similar mismatches of stratal thickness and displacement across faults are observed on faults F3c and F3d. The thickest part of the trough fill lies between faults F2 and F3a and contains thin clayey deposits (units 2a and 2b). These were interpreted as basal sag pond deposits, so should have been deposited subhorizontally. But at present they are tilted down-to-

357 the-south as much as 50°-60°. This degree of tilt is even greater than the 30°-40° southward tilt
 358 of strata in the rotated block in the south end of the trench.

359
 360 Several lines of evidence indicate that the bedrock surface exposed on the north end and floor
 361 of the trench is the top of a bedrock block that has been rotated clockwise (down-to-the-south).
 362 First, the originally-horizontal sag pond deposits (unit 2) now dip south, which can only have
 363 been caused by rotation down-to-the-south (not by outward toppling to the north). Second, with
 364 successive rotation the trough deepened, which was accompanied by normal faulting on the
 365 south margin of the trough (seen in unit 3) and sliding of blocks of exotic stratigraphy into the
 366 trough. Third, the presence of two reverse faults (F2, F3b) is an anomaly in a system of rotating
 367 domino blocks, normally associated with extension.

368
 369 *Interpreted Sequence of Deformation:* Based on stratigraphic superposition, cross-cutting
 370 relationships, and the occurrence of two paleosols, we interpret a sequence of four late
 371 Quaternary deformation events at Trench 1, with two more questionable events (Table 1).

372
 373 Table 4. Inferred sequence of depositional, pedogenic, and deformational events affecting
 374 Trench 1.

Event (oldest at bottom)	Evidence
11-Deposit units 5b, 5aAC, 6A	A 1.3 m-thick fining-upward sequence (5b-5a-6) is deposited as wash-facies colluvium (slopewash), on which is developed a thickcumulic surface soil (horizons6A, 5aAC). Lower unit 6A yields charcoal age of 1014-1235 calBP .
10-Deformation EVENT Z	Youngest event faults unit 5b against unit 4 on fault F1; faults unit 4 on faults F1 and F3d. Fault F2 faults unit 4 up to N, but offsets unit 2a down-to-N
9-Deposit unit 4	Followed by accumulation of organic material in an A horizon Paleosol; ; 3139-3436 cal BP
5-Deformation EVENT Y	Unit 3 is faulted. Between faults F2 and F3a all of unit 3 is translated away, either westward by oblique faulting, or it all slides southward to its present location.
4-Deposit unit 3	Fine-grained units 2a-2b are abruptly buried by coarser colluvial units 3a (derived from the north) and 3b-3f (derived from the south).
3-Deformation EVENT X	Trough deepens due to faulting and clockwise block rotation.
2-Deposit units 2a, 2b	Thin sag pond silts and clays (2a, 2b) accumulate in trough; reduced conditions.
1-Deformation EVENT W	Normal faulting creates the initial topographic trough

375
 376
 377 *4.4 Trench 2*

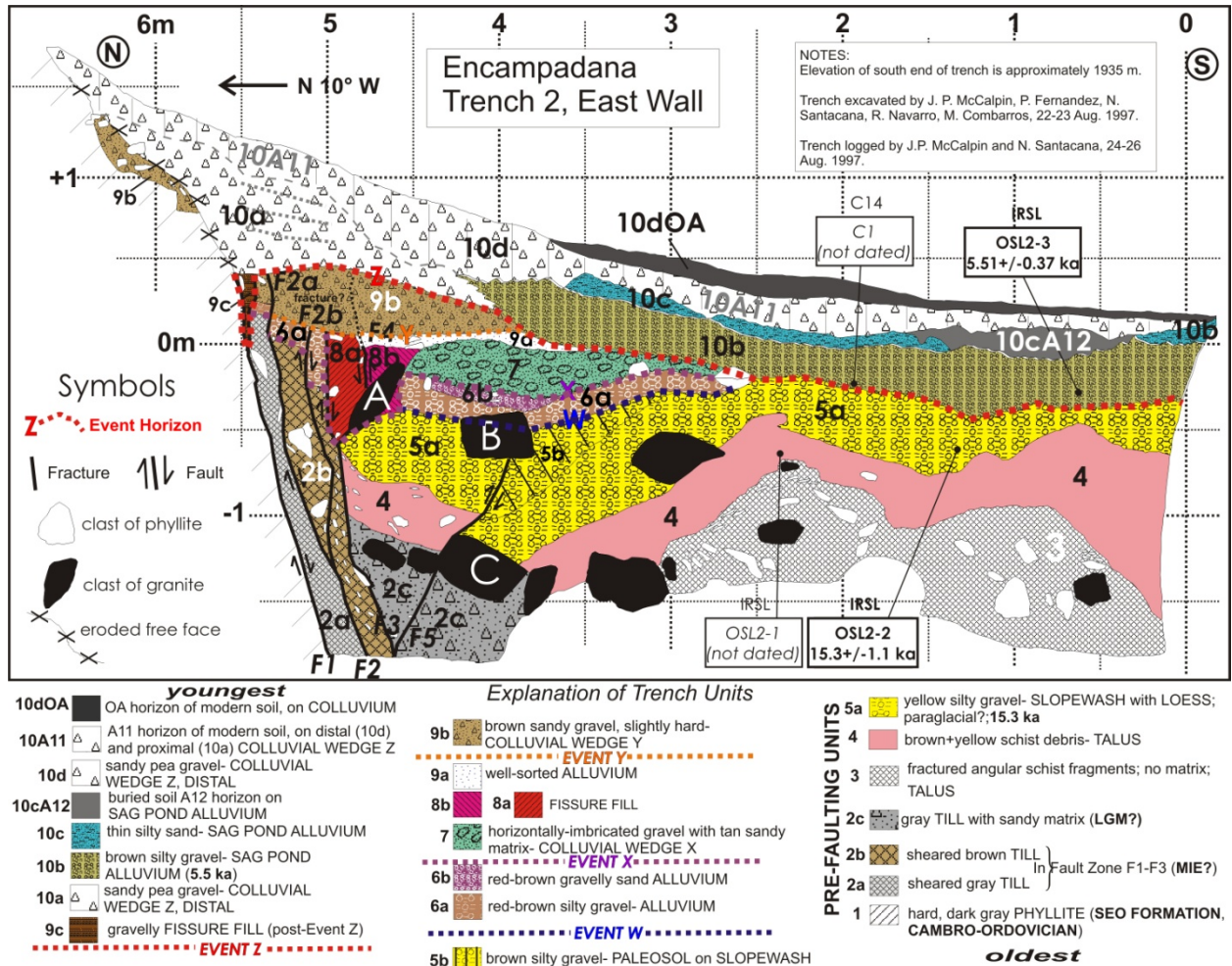
378 Trench 2 was located at 1935 m elevation on the lowest-elevation antislope scarp in the
 379 Encampadana complex, only 300 m above the modern valley floor (Fig. 5). Trench 2 was the
 380 longest (6 m) and deepest (3 m of stratigraphic section) of our three hand-dug trenches. The
 381 trench axis was oriented N10°W, perpendicular to the sackung trough.

382
 383 *Local Geomorphology:*The trenched antislope scarp/trough is a roughly 500 m long and follows
 384 foliation to the WNW, cutting obliquely across contours that trend WSW. Downslope of this
 385 scarp all the mapped scarps face downslope and appear to be part of a late Holocene landslide
 386 on the oversteepened lower valley wall.

387
 388 *Stratigraphy and Soils:* On the east wall we define 10 major units, which were further subdivided
 389 into 23 subunits (Fig. 9). The oldest units (1-5) maintain a tabular geometry throughout the
 390 trench, suggesting that they were either: (1) deposited on a uniform slope unaffected by
 391 development of a sackung trough and scarp (“Pre-Faulting Units” on Fig. 8), or (2) deposited in
 392 a trough much wider and shallower than the present trough. In contrast, units 6-10 are lenticular
 393 and are restricted to the northern half of the trench. Each of these five units is located above the

394
395
396

axis of maximum displacement on faults that were active before its deposition. Thus we interpret units 6-10 as deposits that accumulated between successive deformation events.



397
398
399

Fig. 8. Log of the east wall of Trench 2.

400
401
402
403
404
405
406
407
408
409
410
411
412
413
414
415

The oldest deposit exposed in the trench (unit 1) is the hard, dark gray phyllite of the Seo Formation (Cambro-Ordovician) that underlies the lower half of the Encampadana slope. This bedrock unit is only exposed on the footwall of the main south-dipping normal fault beneath the sackung scarp. The oldest in-situ unconsolidated deposit (unit 2c) is a gray, unoxidized till exposed in the deepest part of the trench. The till contains exotic subrounded clasts of granite derived from far upvalley of the Encampadana slope, indicating it was deposited here by the Valira d'Orient glacier. Material derived from this till has been drug up along the main fault zone (units 2a, 2b). In the southern half of the trench the oldest deposit (unit 3) is composed of angular schist and phyllite fragments with no matrix. This deposit contains no granite and appears to be a locally-derived talus deposit, age equivalent to (or slightly younger than) the gray till. Overlying units 2c and 3 is a brown, oxidized talus deposit (unit 4) similar in lithology to unit 3. This talus fines upward into a poorly-sorted yellow silty gravel (unit 5a), the upper part of which has been turned brown by soil formation (unit 5b, and paleosol). The base of unit 5a yielded an IRSL age of 15.3±1.1 ka, suggesting it was deposited shortly after the retreat of the LGM glacier. The silt content may be loess deflated from the retreating outwash plain.

416 Units 6 through 10 comprise 15 subunits comprised of one of these facies: (1) thin, tabular, well-
 417 sorted alluvium, (2) coarser lenses or wedges of poorly-sorted colluvium, and (3) downward-
 418 tapering wedges of poorly sorted fissure fill. These facies are all located above deformation
 419 structures in the trench, and are interpreted as alluvial and colluvial deposits, respectively, that
 420 accumulated episodically in the sacking trough. Unit 10 is the largest of these deposits and
 421 contains scarp-derived colluvium (10a) and correlative sag-pond alluvium (10b; basal age
 422 5.51 ± 0.37 ka), overlain by thin alluvium and a paleosol (units 10c and 10cA12, respectively),
 423 distal wash-facies colluvium (10d) and its two soil horizons (10A11 and 10dOA). None of these
 424 subunits are deformed, indicating that all deformation occurred after 15.3 ka but before 5.5 ka.

425
 426 *Structure:* Trench 2 structures are mainly normal faults, numbered from the footwall to the
 427 hanging wall as F1, F2 (F2a, F2b), F3, F4, and F5. Faults F1 through F3 are steeply south-
 428 dipping normal faults in the main fault zone that underlies (and created) the south-facing
 429 sackung scarp (Fig. 9). The fault sliver between F1 and F2 is filled with unoxidized gray sheared
 430 till, clearly derived from unit 2c. The sliver between F2 and F3 is filled with an oxidized brown
 431 sheared till. F4 is a subvertical fault that splays upward from F3 and bounds the south edge of a
 432 fissure fill (unit 8a). F5 is a north-dipping fault that displaces the hanging-wall sequence down-
 433 to-the-south in an apparent reverse sense. We suspect that some local horizontal compression
 434 was generated here by the down-to-the-north rotation of units 3-6 between 2.5 m and 4 m on
 435 the horizontal grid. As in Trench 1, the down-to-the-north rotation of those units tends to push
 436 them northward into their correlatives on the north side of the fault, putting that area into
 437 compression.

438

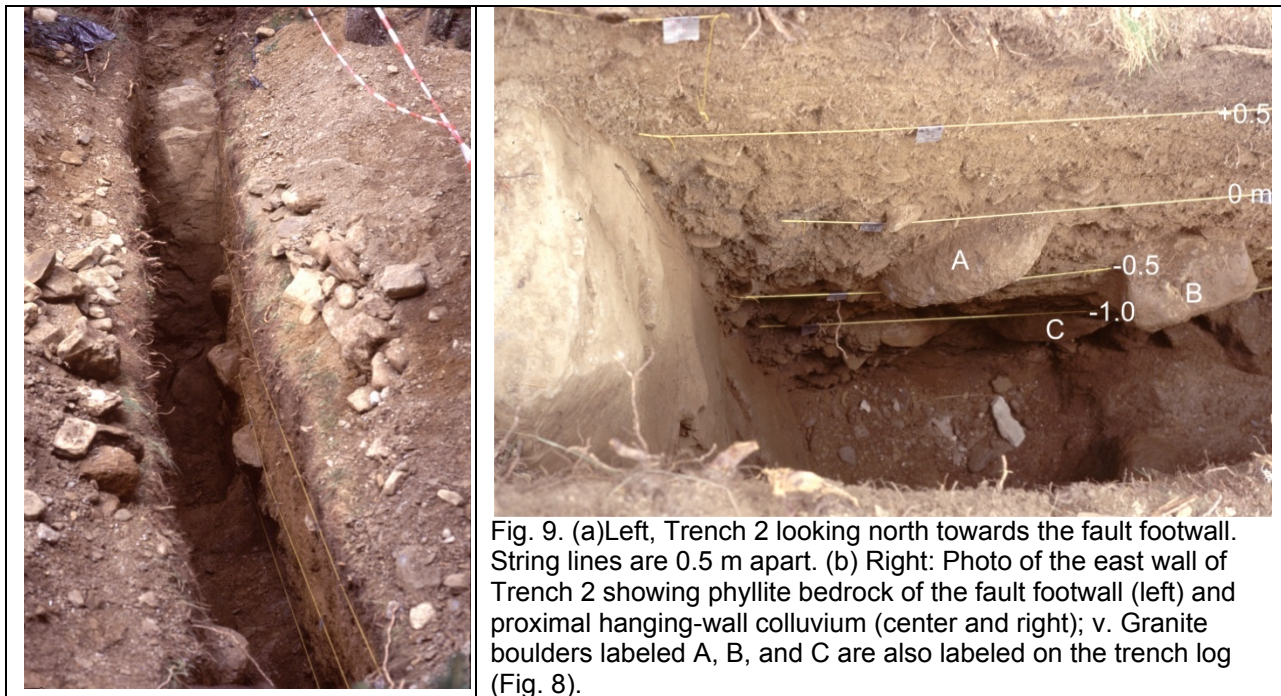


Fig. 9. (a) Left, Trench 2 looking north towards the fault footwall. String lines are 0.5 m apart. (b) Right: Photo of the east wall of Trench 2 showing phyllite bedrock of the fault footwall (left) and proximal hanging-wall colluvium (center and right); v. Granite boulders labeled A, B, and C are also labeled on the trench log (Fig. 8).

439

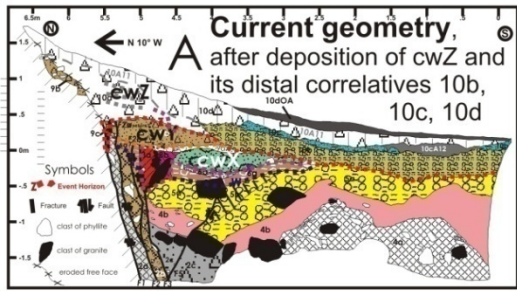
440

441 *Interpreted Sequence of Deformation:* The number of deformation events at Trench 2 is
 442 evaluated via a retrodeformation sequence (Fig. 10). The sequence starts (Stage A) with the
 443 present trench wall geometry and proceeds backwards in time, by a stepwise: (1) removal of
 444 any unfaulted deposits, and (2) reversing the fault movement such that the youngest underlying
 445 faulted deposits are restored to their continuous (pre-faulting) geometry. Then these deposits

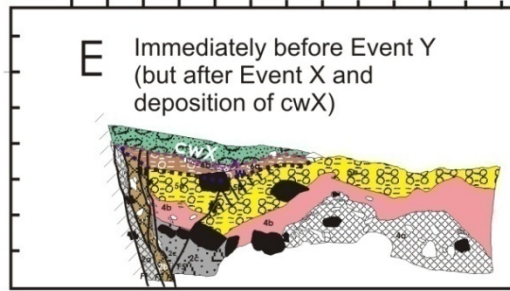
446 are removed, and so on to Stage G (geometry of Quaternary deposits before trough formation).
447 This procedure recognizes all upward fault terminations in the stratigraphic sequence, which
448 occur at unconformities separating faulted from unfaulted strata. In paleoseismic investigations
449 such unconformities created by coseismic faulting events are termed “event horizons”, a term
450 which we will use in this paper, but not implying in any way that the deformation events are
451 related to earthquakes.

452
453 We recognize four event horizons in Trench 2, labeled from Z (youngest) to W (oldest). Event
454 horizons Z, Y, and X coincide with scarp-derived colluvial wedges (cwZ, cwY, and cwX
455 respectively) overlying either older wedges or inter-faulting alluvium. The next older event
456 horizon (W) resulted from downwarping of units 3-5 into a narrow trough, quickly followed by
457 alluvial erosion then deposition (units 6a, 6b) in the trough axis. The lack of a colluvial wedge
458 following Event W suggests that no high scarp was formed in this event, but only an extensional
459 fissure. Event W occurred long enough after 15.3 ± 1.1 ka that a weak paleosol (unit 5b) had
460 formed on the pre-faulting colluvium. Subsequent downwarping of units 6a and 6b beneath unit
461 7 (colluvial wedge X) suggest further sagging occurred in Event X. The latest deformation event
462 (Z) occurred immediately before deposition of unfaulted unit 10b at 5.51 ± 0.37 ka. Thus, all four
463 deformation events occurred in a time span of <10 ka (<15.3 to 5.5 ka). In addition, it is possible
464 that units 2 through 5 were deposited in a pre-existing depression, rather than on a uniform
465 erosional slope. However, our trench exposure was too limited in size to distinguish these two
466 possibilities.

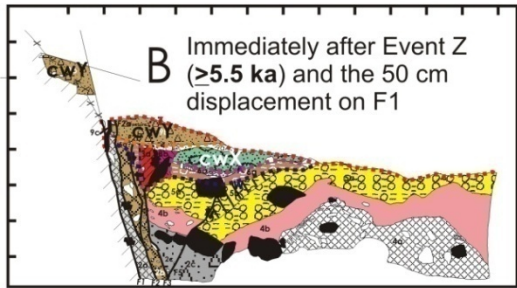
467
468



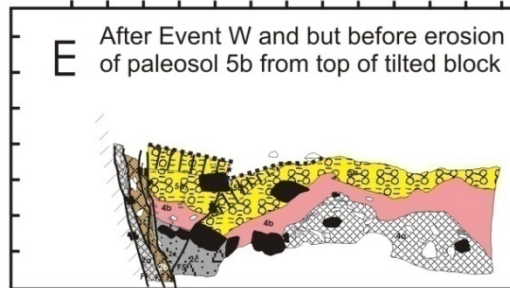
↓ delete youngest wedge (cwZ);
restore prev faulted wedge (cwY)



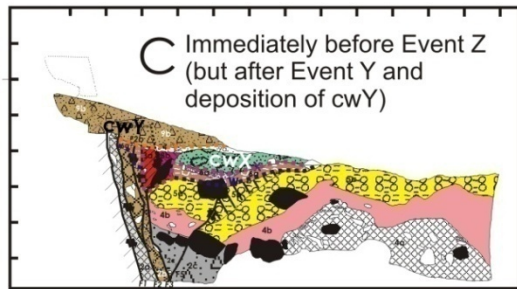
↓ delete wedge cwX and 6a
restore top of faulted block and paleosol



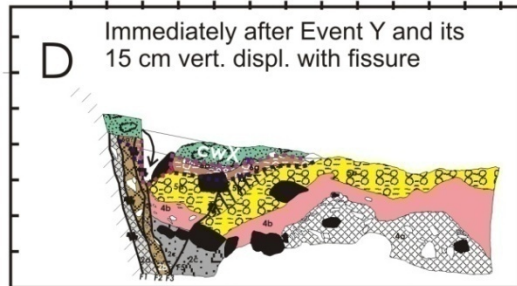
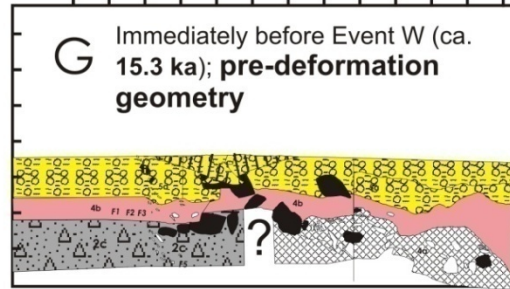
↓ reverse fault movement;
restore wedge cwY to one piece



↓ reverse fault movement
restore pre-faulting geometry



↓ delete wedge cwY;
restore prev faulted wedge cwX



↓ reverse fault movement;
restore wedge cwX and 6a
to one piece

469
470
471
472
473
474

Fig. 10. Retrodeformation sequence of the East Wall of Trench 2. Stage A represents the present trench wall geometry, Stage G the geometry prior to Event W. There may have been additional sacking events prior to Event W, but our trench was not long enough or deep enough to permit reconstruction of the topography of that time.

475 **4.5 Trench 3**

476 Trench 3 was located at 2320 m elevation on the highest-elevation antislope scarp/trough pair in
477 the Encampadana complex (Fig. 5). The trench was 5 m long and up to 2 m deep, oriented
478 toward N10°E (perpendicular to the trough axis).

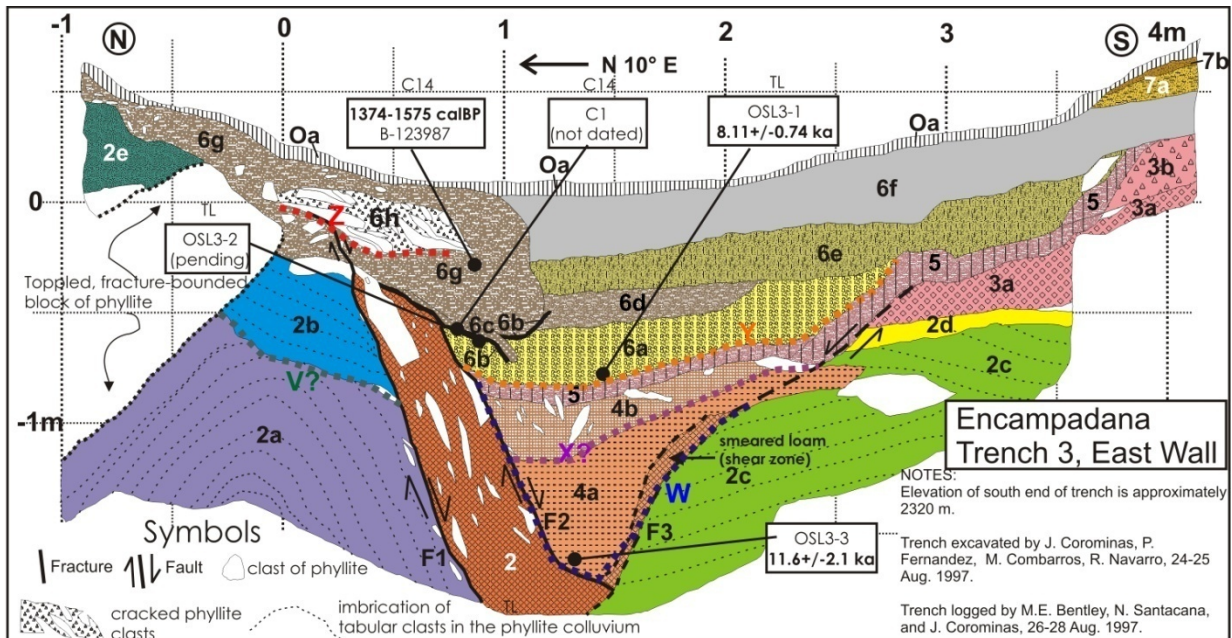
479

480 *Local Geomorphology:* Trench 3 crosses the axis of a ~5 m-wide trough which is
481 topographically closed at the trench site (Fig. 11). We chose the site hoping to expose fine sag-
482 pond sediments beneath the center of the closed trough, which might be suitable for C-14
483 and/or IRSL dating. The trough margins are asymmetrical, with the northern boundary being
484 formed by a 2 m-high near-vertical outcrop of Devonian phyllite, while the southern boundary is
485 a gentler grassy slope underlain by inactive talus.
486



487 Fig. 11. Site of trench 3. (a) Left, site before trenching, view to NE. Trench was dug between two red
488 arrows. (b) Right, view of trench 3 looking N.
489

490 *Stratigraphy and Soils:* On the east wall we define 7 major units, which were further subdivided
491 into 22 subunits (Fig. 12). The oldest unit (1) is phyllite bedrock (Devonian) of the fault footwall.
492 The oldest unconsolidated deposit exposed is unit 2, mainly a talus deposit composed of
493 angular fragments of phyllite, either without any matrix (unit 2a) or with a finer sandy matrix (2b,
494 2c). The geometry of these deposits does not conform to any of the present structures of
495 topography of the sackung scarp or trough, so we interpret it as pre-trough talus. The shear
496 zone that truncates units 2a and 2b is labeled unit 2. Younger talus of the hanging wall
497 comprises unit 3. Unit 4a is a fine-grained deposit (silty clay) that fills a paleo-depression
498 against the shear zone and is the oldest unit with sedimentology consistent with deposition in a
499 closed depression. The base of unit 4a yielded an IRSL age of 11.6 ± 2.1 ka, a close minimum
500 age estimate for inception of the sackung trough. Unit 4a is unconformably overlain by a
501 southward-tapering wedge of much coarser silty clay loam with angular clasts (unit 4b),
502 interpreted as scarp-derived colluvium. Unit 5 is a paleosol developed on unit 4b, and to the
503 south, on units 2d, 3a, and 3b. On the latter units it appears to be developed in a separate, silty
504 (loess-rich?) parent material. [Unit 5 strongly resembles the unit 4 paleosol exposed in Trench
505 1, which is also a thin dark brown silty loam that blankets multiple units]. The unit 5 paleosol is
506 unconformably overlain by a second fining-upward of fine-grained sag pond deposits (units 6a
507 through 6f) capped by a paleosol. The bottom of unit 6 yielded an IRSL age of 8.11 ± 0.74 ka. In
508 the center of the topographic trough the A horizon of this soil (unit 6f) is the surface soil. But on
509 the northern and southern flanks of the trough unit 6f is overlain by younger deposits (6g and 6h
510 on the north, 7a and 7b on the south). The center of unit 6g yielded a radiocarbon age of 1374-
511 1575 cal BP.
512



youngest		Explanation of Trench Units	
OA	Organic A horizon	5	PALEOSOL; developed on dark gold-brown silty clay loam (loess?)
7b	brown loam	4b	reddish-brown silty clay loam with angular clasts, COLLUVIUM
7a	yellow brown silty loam	4a	reddish-brown silty clay loam, rare clasts, SAG POND SILT (11.6 ka)
6h	cracked phyllite clasts	3b	coarse phyllite TALUS without matrix
EVENT Z		3a	phyllite TALUS with opposite imbrication to above
6g	dark brown silty loam	2e	phyllite TALUS on the upthrown block
6f	A horizon (grayish brown sandy silt)	2d	sandy silt ("Jordi's bed")
6e	B horizon (mottled yellow-brown silty clay loam)	2c	phyllite TALUS with some matrix
6d	brown silty loam	2b	phyllite TALUS with some dark brown clay matrix
6c	dark brown clay	2a	phyllite TALUS
6b	black to d. brown silt (burn layer?)	2	SHEAR ZONE with reddish-brown silty clay loam matrix
6a	yellow-brown gravelly silty loam; 8.1 ka		
EVENT Y			oldest

514

515

Fig. 12. Log of the east wall of Trench 3. As at Trench 2, the oldest deposits here (unit 2, talus) may have been deposited in an older sacking trough rather than on an undeformed slope. But our limited exposure precludes testing such a hypothesis.

516

517

518

519

Structure: The trough margins are underlain by inward-dipping normal faults. The northern faults (F1, F2) bracket a 20 cm-thick shear zone (unit 2) containing fault-parallel, tabular clasts of phyllite in a matrix of reddish-brown silty clay loam. Based on color and texture, this matrix was derived mainly units 4a and 4b, although there may have a small component from units 5 and 6a. The southern fault (F3) has a narrower shear zone (10 cm) and less overall vertical displacement (28 cm) than faults F1+F2. The youngest deformation in the trench occurred where fault F1 propagated upward and displaced the lower half of unit 6g.

520

521

522

523

524

525

526

527

In addition to these major extensional structures, there are minor compressional structures. The northern end of the trench exposes an isolated block of phyllite that has toppled southward toward the trough axis. Toppling opened a small void space on the north side of the block, into which unit 2e was deposited. However, on the south side of the block, stratified talus of unit 2a has been folded into an anticline, indicating local compression. Likewise, the antithetic normal fault F3 now has a rather serpentine shape, as if the originally planar fault was bent by unit 2c pushing northward toward the trough axis.

528

529

530

531

532

533

534

535

536 *Interpreted Sequence of Deformation:* Based on stratigraphic superposition, cross-cutting
 537 relationships, and the occurrence of two paleosols, we interpret a sequence of three late
 538 Quaternary deformation events at Trench 3, with a questionable 4th event (Table 5).
 539

540 Table 5. Inferred sequence of depositional, pedogenic, and deformational events affecting
 541 Trench 3.

Event (oldest at bottom)	Evidence
10-Deformation EVENT Z	On fault F2, the north margin of unit 6a is sheared against unit 2. On fault F1, a small-displacement fault propagates upward through the lower half of unit 6g.
9-Deposit unit 6	A 0.9 m-thick fining-upward sequence (6a-6d) with a 0.25- m surface soil (A horizon, unit 6f; B horizon, unit 6e). On north side of trough all subunits are intruded by a solifluction (?) lobe with a basal burn layer.
8-Deformation EVENT Y	Displaces unit 5 paleosol up 0.5 m to south; forms shear zone at unit 4a/2c contact; deepens trough.
7-Deposit units 4b, 5	Unit 4b has a sharp contact with underlying unit 4a and is much coarser; but could be either a colluvial wedge (tapers to south) or debris flow. In contrast, unit 5 is a paleosol (represents hiatus) on slope-mantling loess.
6-Deformation EVENT X?	Questionable deformation event. Depends on whether stony unit 4b is a scarp-derived colluvial wedge, or a debris flow.
5-Deposit sag pond silt in trough	Sag pond silt (unit 4a) has no correlatives outside of the inner trough (i.e., south of fault F3).
4-Deformation EVENT W	Extensional faulting/fissuring on faults F1-2-3 creates a narrow topographic trough.
3-Deposit units 2b, 2c, 2d, 3a, 3b	Talus sourced from the south
2-Deformation EVENT V?	Unconformity on footwall; unit 2a talus is folded into an anticline, but overlying unit 2b talus is not folded. Possibly not due to deformation; could be depositional?
1-Deposit unit 2a TALUS	Source is upslope to the South

542

543

544 6. Discussion

545 Our three trenches sampled only three of the ~50 antislope scarps on the northern slope, so our
 546 interpretation of the larger pattern of slope kinematics may be viewed as preliminary. However,
 547 we do see some trends that we believe can be generalized over the entire deforming slope.

548

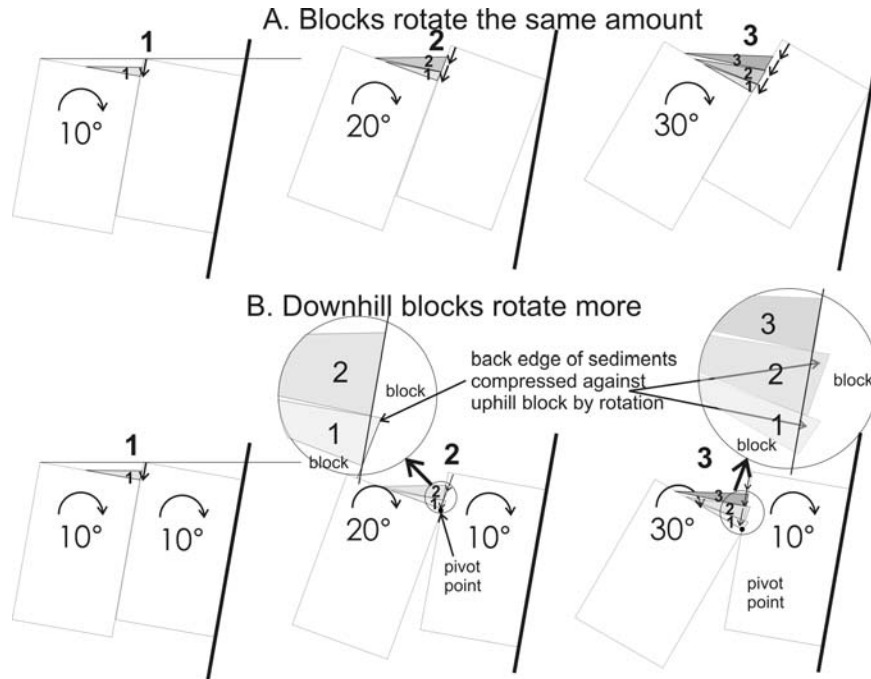
549 6.1 Reconciling Extensional and Compressional Structures in a Single Trench

550 The conventional explanation of DSGSD is that it accommodates valleyward movement mainly
 551 by toppling (**need References**), which is essentially an extensional process. Our trenches show
 552 dominantly extensional structures, but each one also contains minor compressional structures
 553 (reverse faults and folds). Does this mean that the entire gravitational stress field on the
 554 mountain slope is switching from extension to compression and back to extension? Or does it
 555 reflect a very local response to changing subsurface geometry as the sackung slope elements
 556 rotate and evolve? We believe the latter, for reasons explained below.

557

558 Trench 1: This trench shows some small-displacement reverse faults in the lower part of the
 559 trough fill, as well as horizontal ‘squeezing’ of the unit 4 paleosol to attain slopes exceeding the
 560 angle of repose. Our first thought was that horizontal compression was caused by slump blocks
 561 (unit 3) sliding into the trough from upslope. The toes of such slump blocks would press against
 562 the sediments already deposited in the trough, causing local compression. However, such
 563 compression should also deform the toe of the slide block, and strata in the supposed slide
 564 block (unit 3) are not so deformed. Another possible source of compression would arise if
 565 adjacent bedrock blocks rotated a different amount, which would cause compression in the back
 566 edge of the sediment wedge. As long as two adjacent ‘domino blocks’ rotate the same amount,
 567 the fault movement along their boundary fault will be purely translational (i.e., a normal fault;
 568 Fig. 13A). However, if the downhill block rotates more than the uphill block, the sediment wedge

569 (which sits atop the downhill block) will also be rotated (Fig. 13B). That rotation, even across a
 570 pivot point located on the fault, will pivot the sediment wedge into the uphill block, such that the
 571 back edge of the wedge will be forced into the uphill block, trying to occupy the same space.
 572 The result will be compressional deformation of the softer trough sediments, and this will
 573 increase as the difference in rotation angle increases.
 574



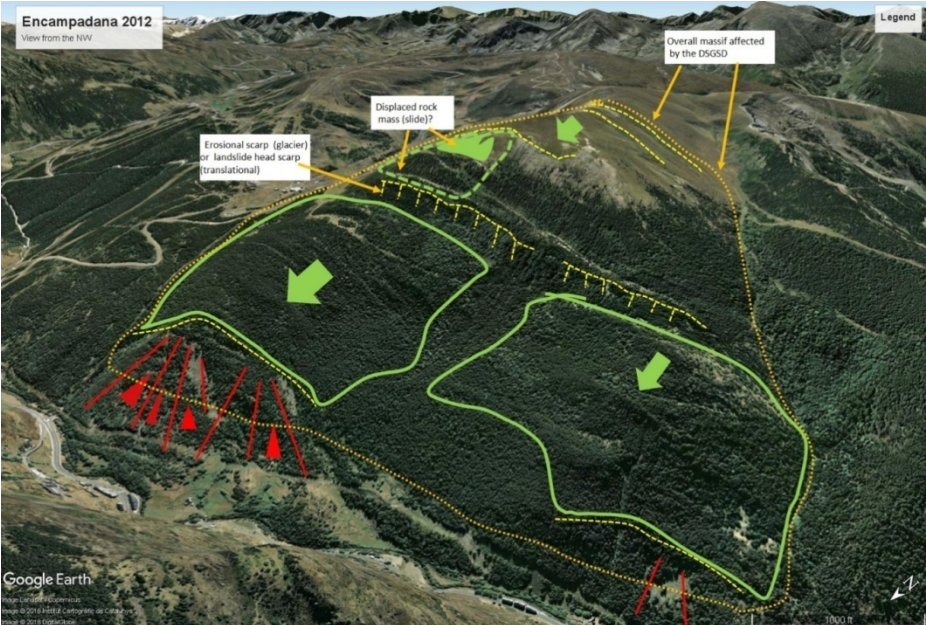
575 Fig. 13. Schematic diagrams of a pair of gravitationally-rotated bedrock blocks where sediments fill the
 576 trough created by rotation. (A), both blocks rotate the same amount through time; sediment wedges 1, 2,
 577 and 3 (gray shades) accumulate. (B), the downhill block rotates more than the uphill block, using a
 578 pivot point on the fault plane where the two blocks touch (small black circle). As the difference in rotation
 579 increases, the back edge of the earlier sediment wedges gets pushed horizontally into the uphill bedrock
 580 block, inducing compression in the trough sediments.
 581
 582

583 **Trench 2:** Trench 2 contains a master south-dipping normal fault with a smaller north-dipping
 584 reverse fault splaying upward into the hanging wall sediments (Fig.8). Secondary reverse faults
 585 have been documented in the hanging wall of historic normal fault scarps (e.g., Crone et al.,
 586 1987) and observed in many paleoseismic trenches across tectonic normal faults (McCalpin,
 587 2009, p. 215-219). The causes may range from upward fault refraction (in response to
 588 decreasing confining pressures near the surface, to a piece of the hanging wall sediments
 589 getting cemented to the fault plane, and thus attached to the footwall in succeeding
 590 displacements. Neither explanation seems applicable to the reverse fault in Trench 2. Instead,
 591 the reverse fault is contiguous with a section of hanging-wall sediments that were rotated down
 592 toward the master normal fault. Units 3 (?), 4 and 5a appear to compose a domino block that
 593 has rotated down-to-the-north, toward the reverse fault. As at Trench 1, this rotation would force
 594 the north-dipping units 3-5a to try to occupy the same space as their south-dipping relative
 595 farther north, leading to compression. An alternative explanation would invoke localized
 596 collapse into a void space to explain the northward dip of units 3-5a. In that scenario units 3-5a
 597 between 2.5-4 m on the grid are sagging downward into a subsurface void, perhaps created by
 598 fault refraction of the master normal fault in Event W. But for some reason the northernmost
 599 parts of units 3-5a have been cemented to the main shear zone, so they have moved upward as
 600 part of the footwall, at the same time that their counterparts farther south have collapsed

601 downward into the void space. This differential movement has created a fault with the sense of
602 a reverse fault, but with no horizontal compression involved.

603
604 Trench 3: During logging of Trench 3 we assumed that the anticlinal folding of unit 2a was
605 entirely caused by slow forward toppling of the phyllite block. However, the upper part of the
606 toppled block lies against unit 2b, which is not folded. So it seems that, in this trench, a more
607 far-field source of compression may be required. In the southern half of the trench, normal fault
608 F3 contains an anomalous northward bulge, a very odd shape for a tensional fault. Northward
609 slippage along bedding planes in unit 2c could explain that bulge, but such slippage would
610 require compression coming from outside of the trench, somewhere up the slope to the south.
611 Both deformation structures appear to be plastic deformation of coarse-grained sediments,
612 which suggests slow, creep-style deformation, rather than rapid, episodic (brittle) deformation.
613 As shown in Fig. 14, upslope of trench 3 there is a large downhill facing scarp. A rock wedge is
614 located between this scarp and the footwall of trench 3. So a possible source of far-field
615 compression is that this rock wedge has slid down and compressed the entire area around
616 Trench 3.

617



618
619 Fig. 14. Overall view of the Encampadana massif. In the foreground (red color) scree deposits (the local
620 place name here is El Tarter, meaning “scree”). The longest scarp at mid-slope (yellow dashed line)
621 suggests that in addition to toppling some translational movement has occurred (green arrows). Upslope
622 of the long scarp lies a smaller, inferred displaced rock mass. Trench 3 lies in the downslope half of this
623 rock mass.

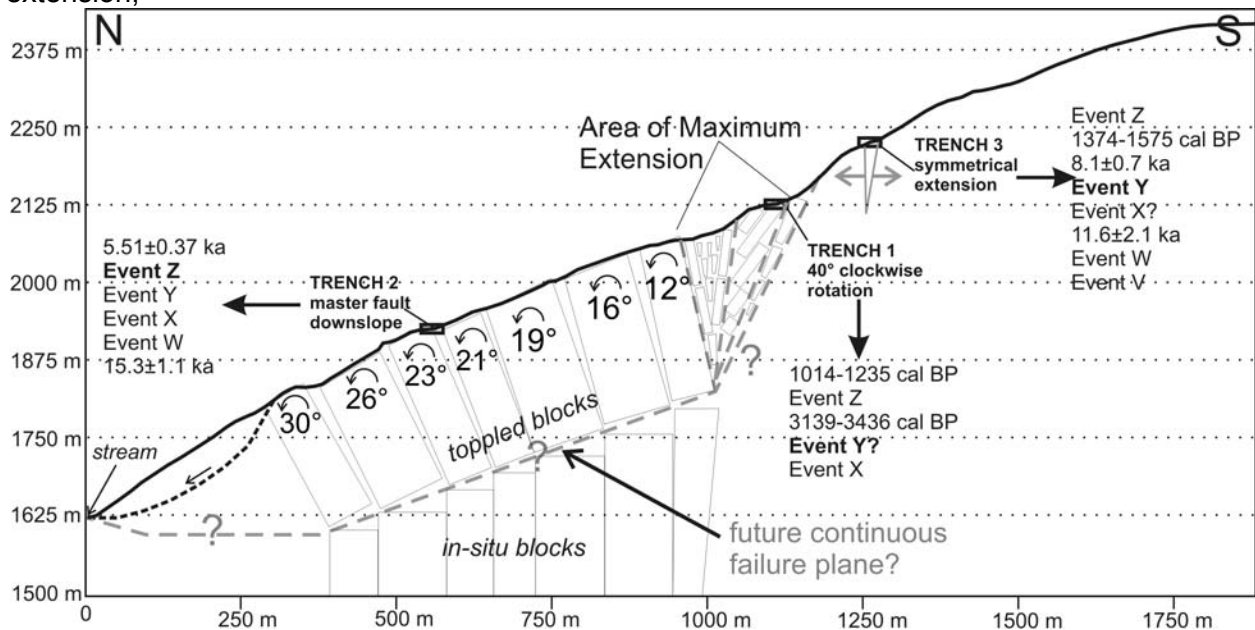
624
625
626 The timing of compressional deformation is also different among the trenches. In Trench 1
627 reverse faulting and folding accompanied the youngest displacement (Event Z), affecting units
628 at least as young as 3.2-3.4 ka. In Trench 2 the reverse fault is much older, moving only in the
629 oldest of the four recognized displacement events (Event W, slightly younger than 15.3 ka).
630 Compressional deformation in Trench 3 is also old, affecting only units older than 6a, which is
631 8.1 ka. The cessation of compressional deformation thus varies widely among the trenches, so
632 much that it cannot represent a mountain-wide change in the stress field, but rather some more
633 localized phenomenon.

634

635 **6.2 Evolution of Deformation over the Whole Slope at Encampadana**

636 Our trench geochronologies indicate that antislope scarps and troughs first formed low on the
 637 slope (Trench 2) by 15.3 ka, but deformation there had stopped prior to 5.5 ka. At the midslope
 638 position (Trench 1) deformation continued until later, with the latest event (Z) just after 3139-
 639 3436 cal BP. Farther up the slope (Trench 3) the latest event (Z) was even younger, occurring
 640 after 1374-1575 cal BP. In addition, there are morphologic indicators of displaced rock masses
 641 and downhill-facing scarps farther upslope of Trench 3. Taking into account the structural style
 642 of deformation in each trench and the timing of deformation events, we have constructed a
 643 schematic cross-section through the northern slope of Encampadana (Fig. 15). This cross-
 644 section makes several assumptions:

- 645 (1) the pervasive antislope scarps in the downhill half of the section were created by bedrock
 646 blocks, bounded by subvertical foliation planes, that have toppled valleyward;
 647 (2) the top of each toppled block is parallel to today's ground surface;
 648 (3) the resulting amount of toppling is greater toward the toe of the slope. This could be because
 649 slope deformation started earlier there (as indicated by trench geochronologies);
 650 (4) the steep, long scarps in the midslope position reflect an area of localized maximum
 651 extension;



652 Fig. 15. Interpretive cross-section through the northern slope passing through trenches 1, 2, and 3. Thick
 653 arrows point to the chronology of deformation Events interpreted for each trench, and numerical ages
 654 from each trench. The Event with the largest vertical displacement is shown in bold.
 655
 656

- 657 (5) this extension has created the severely-back-rotated blocks seen in Trench 1;
 658 (6) in order to achieve such large extensions at the surface, there must be at least an incipient
 659 discontinuity between the bottom of the toppled blocks and in-situ bedrock;
 660 (7) the depth of that discontinuity can be approximated at its uphill end by projecting downward
 661 the bounding faults in the area of maximum extension;
 662 (8) the downhill end of the potential discontinuity should not be too far below the present (post-
 663 glacial) valley floor; and
 664 (9) the relatively small, asymmetrical extension seen in Trench 3 suggests it lies outside of the
 665 main zone of slope deformation, but perhaps responding to extension from the major
 666 gravitational unloading just downslope.

667

668 Other authors have documented similar spatial-temporal trends in DSGSD. In one of the earliest
669 sackung trenching studies McCalpin and Irvine (1995) speculated that antislope scarps would
670 be younger the higher above the glacial trimline, based on the ~2.5-4 kyr lag time between
671 deglaciation and initiation of the highest scarp at the ridge crest. Hippolyte et al., 2009
672 concluded: *“This decrease of the age of the scarps with elevation much probably reflects the*
673 *propagation of the deformation toward the crest (from elevation 2190 m to 2419 m)... This*
674 *chronology agrees with the proposed mechanism of flexural toppling. The migration of the slope*
675 *deformation from the valley flank to the crest also supports the model of glacial debuttressing for*
676 *the origin of the Arcs sackung.”* El Bedoui et al. (2009, 2011) observed a similar trend on the La
677 Clapiere slope in the French Alps. Panek et al. (2017) concluded *“In general, we observe a*
678 *statistically significant correlation showing a progressive decrease of sackung scarp ages with*
679 *their increasing altitudinal position... Such a relationship might indicate linkage of (delayed)*
680 *sackung genesis to overall thinning and retreat of glaciers since the LGM... Therefore, slow*
681 *upslope migration of stress release after glacier withdrawal... could partly explain substantial*
682 *time lag of a number of sackung scarps.”* Panek et al. (2017, their Fig. 5) showed a cross-
683 section similar to our Fig. 15, with age control coming from ¹⁰Be dating of rock exposed on the
684 sackung scarp face. Their oldest dated antislope scarp was the lowest one, as at
685 Encampadana. However, the next-youngest scarp was at the head of the slope (analogous to
686 the Solanelles graben at Encampadana), and the youngest scarps were in the midslope
687 position. Thus, in hindsight, it appears should have also trenched the margin scarps of the
688 Solanelles graben in order to capture the entire span of slope deformation. We considered this
689 in our initial field reconnaissance, but the graben surface there showed no discrete sediment
690 traps and did not look promising for dating fine-grained deposits. Instead, the entire surface was
691 covered with large-diameter frost-shattered slabs and rubble of phyllite.

692

693 **7. Conclusions**

694 Sackung troughs formed at Encampadana have acted as sediment traps since formation, and
695 are underlain by distinctive postfaulting strata that permit reconstructing the evolution of the
696 antislope scarp and adjacent trough. The oldest strata exposed in our 2-2.5 m-deep trenches
697 are coarse, angular talus deposited as either slope-mantling sediments that predate the modern
698 sackung scarp and trough, or as sediments trapped in a very wide and shallow trough of
699 unknown origin. These deposits have been disrupted by normal and reverse faulting, with the
700 largest fault zone underlying the antislope scarp and dipping south at 40°-80°. Each trench
701 contains subsidiary north-dipping normal faults beneath the southern edge of the trough, giving
702 the appearance of a graben. However, in two of three trenches post-faulting deposits have
703 subsequently been tilted or folded down toward the main fault, as if sagging into a void space
704 created by horizontal extension and/or outward toppling of the footwall. The trough fill is
705 generally dominated by poorly-sorted sandy slopewash, but does contain two other important
706 facies: (1) thin clay and silt deposits deposited in standing water, found beneath the center of
707 the trough, and (2) gravelly scarp-derived colluvial wedges, found beneath the edges of the
708 trough. Paleosols have formed on the top of fining-upward sequences of strata, permitting
709 interpretation of several cycles of: (1) episodic downdropping along graben faults and
710 deepening of the topographic trough, (2) filling the trough with marginal colluvial and axial sag-
711 pond sediments, followed by (3) a hiatus of soil profile development. The structures and inter-
712 faulting sedimentation patterns are very similar to those exposed in trenches across active
713 normal faults (e.g. McCalpin, 2009, Chapter 3).

714

715 Despite their shallow depths, each trench preserves evidence of multiple unconformities and 3
716 to 5 deformation events. Deformation events were recognized by upward termination of faults at
717 various stratigraphic levels, by angular unconformities between trough infill units or fining-
718 upward packages, and by coarse, angular colluvial deposits that thin away from the footwall

719 (scarp-derived colluvial wedges). The average time span between deformation events in any
720 one trench in the past 12-15 ka is about 3-3.5 ka (e.g., in Trench 2, four events between 15.3 ka
721 and 5.5 ka; in Trench 3, successive events at 11.6 ka and 8.1 ka). Deformation seems to have
722 begun first in the lower part of the northern slope (vicinity of Trench 2) about 15.3 ka, and had
723 spread to the upper parts of the slope (Trench 3) by 11.6 ka. However, deformation in the lower
724 slope ceased after 5.5 ka, but still continued higher on the slope in the mid-late Holocene. The
725 youngest deformation dated (ca. 1.4-1.6 cal ka) occurred in the highest trench on the slope
726 (Trench 3). This pattern of younger deformation with increasing elevation has been documented
727 at several other sites (e.g., Panek and Klimes, 2016) and has been ascribed to an upslope-
728 migrating extensional stress field which originated at the base of the slope from glacial
729 oversteepening and end-glacial debuttrussing.

730

731 Subsequent to our field campaign, there have been many published studies in which sacking
732 bedrock scarps were dated by cosmogenic radionuclides (CRN). That type of dating study does
733 not require trenching, which is admittedly difficult in many alpine environments. Although such
734 studies do result in an emergence and exposure history of the bedrock scarps, they do not
735 reveal the various sediment facies within the trough nor their deformation structures, and these
736 are necessary to reconstruct the (at least local) kinematics of DSGD deformation.

737

738 **Acknowledgements**

739 Molly E. Bentley and Nuria Santacana assisted in mapping the trench walls, and field assistants
740 P. Fernandez, M. Combarros, R. Navarro assisted in excavating and backfilling the trenches.
741 IRSL dating was performed by the late Glenn Berger of the Desert Research Institute. Dating
742 and travel support came from National Science Foundation grant EAR-9506371 to Principal
743 Investigator Peter Birkeland at the University of Colorado, Boulder.

744

745 **References**

- 746 Aitken, M.J., 1998. Introduction to Optical Dating. Oxford Univ. Press, Oxford, UK, 256 p.
747 Barnolas, A., Chiron, J.C. 1996. Introduction. Géophysique. Cycle Hercynien. In A. Barnolas
748 and J.C. Chiron (Eds). Synthèse géologique et géophysique des Pyrénées. Editions BRGM-
749 ITGE, vol. 2.
- 750
751 Berger, G.W., 1990. Effectiveness of natural zeroing of the thermoluminescence signal in
752 sediments. J. Geophys. Res. 95, 12,375-12,397.
- 753
754 Berger, G.W., 2000. Optical dating of sediments from Lee Vining (California) & Andorra. Unpub.
755 consulting report submitted to GEO-HAZ Consulting, Inc., Crestone, CO by Luminescence
756 Dating Laboratory, Desert Research Institute, Reno, NV, 04-JAN-2000, 9 p.
- 757
758 Berger, G.W., Lockhart, R.A., Kuo, J., 1987. Regression and error analysis applied to the dose-
759 response curves in thermoluminescence dating. Nuclear Tracks and Radiation Meas. 13, 177-
760 184.
- 761
762 Bordonau, J., Vilaplana, J.M. 1986. Géomorphologie et tectonique récente dans le Val d'Aran
763 (Zone axiale des Pyrénées Centrales, Espagne). Revue de Géologie Dynamique et Géographie
764 Physique, 27: 303-310
- 765
766 Calvet, M., 2004. The Quaternary glaciation of the Pyrenees. In: Ehlers, J., Gibbard, P. (Eds.),
767 Quaternary Glaciations—Extent and Chronology, Part I: Europe. Elsevier, Amsterdam, 119–128
768

769 Calvet, M., Delmas, M., Gunnell, Y., Braucher, R., Bourles, D. 2011. Recent advances in
770 research on Quaternary glaciations in the Pyrenees. In: EHLERS, J., GIBBARD, P. & HUGHES,
771 P. (Eds.), Quaternary glaciations, extent and chronology, A closer look, Part IV. Elsevier,
772 Developments in Quaternary Science, 15, pp. 127–139.,
773

774 Clariana, P. 2004. El sinclinal de Tor-Casamanya. Estudi estratigràfic i estructural. Nova
775 cartografia geològica a escala 1:25.000. A Horitzó núm. 6, Revista del Centre de Recerca en
776 Ciències de la Terra. Institut d'Estudis Andorrans. Andorra la Vella.
777

778 Copons, R., Bordonau, J. 1994. La Pequeña Edad del Hielo en el macizo de la Maladeta (Alta
779 cuenca del Ésera, Pirineos Centrales). In C. Martí-Bono and J.M. García-Ruiz (eds), El
780 Glaciarismo surpirenaico, nuevas aportaciones. Geofoma Ediciones, Logroño. pp. 111-124
781

782 Corominas, J. 1989. Litologías inestables. Monografía nº 3. Sociedad Española de
783 Geomorfología. Zaragoza. pp: 81-96.
784

785 Corominas, J. Baeza, C. 1992. Landslides in the Eastern Pyrenees-Spain. In M. del Prete (Ed):
786 Movimenti franosie metodi di stabilizzazione. Consiglio Nazionale delle Ricerche. Pub. nº 481.
787 Italia. pp.: 25-42
788

789 Crider, J.G., 2001. Oblique slip and the geometry of normal-fault linkage; mechanics and a case
790 study from the Basin and Range in Oregon. J. Str. Geol. 23, 1997-2009.
791

792 Crone, A. J., Machette, M. N., Bonilla, M. G., Lienkaemper, J. J., Pierce, K. L., Scott, W. E., and
793 Bucknam, R. C. ,1987. Surface faulting accompanying the Borah Peak earthquake and
794 segmentation of the Lost River fault, central Idaho. Bull. Seis. Soc. Am. 77, 739–770.
795

796 Delmas M., Calvet, M. Gunnell, Y., Braucher, R., Bourles, D. 2011. Palaeogeography and ¹⁰Be
797 exposure-age chronology of Middle and Late Pleistocene glacier systems in the northern
798 Pyrenees: implications for reconstructing regional palaeoclimates. Palaeogeography,
799 Palaeoclimatology, Palaeoecology, 305, 109–122.
800

801 Delmas, M. 2015. The last maximum extent and subsequent deglaciation of the Pyrenees: an
802 overview or recent research. Cuadernos de Investigación Geográfica, 41: 359-387
803
804

805 El Bedoui, S., Guglielmi, Y., Lebourg, T., Perez, J-L, 2009. Deep-seated failure propagation in a
806 fractured rock slope over 10,000 years: The La Clapiere slope, the south-eastern French Alps.
807 Geomorphology 105, 232-238.
808

809 E; Bedoui, S., Bois, T., Jomard, H., Sanchez, G., Lebourg, T., Trics, E., Guglielmi, Y., Bouissou,
810 S., Chemenda, A., Rolland, Y, Corsini, M., Perez, J-L., 2011. Paraglacial gravitational
811 deformations in the SW Alps: A review of field investigations, ¹⁰Be cosmogenic dating and
812 physical modeling, In Jaboyedoff, M. (ed.), Slope Tectonics, Geol. Soc. London Spec. Pub. 351,
813 11-25.
814

815 García-Ruiz, J.M., Valero-Garcés, B.L., Martí-Bono, C., González-Sampériz, P. 2003.
816 Asynchronicity of maximum glacier advances in the central Spanish Pyrenees. Journal of
817 Quaternary Science, 18: 61-72
818

819 Garcia-Ruiz, J.M., Marti-Bono, C., Valero-Garces, B., Gonzalez-Samperiz, P., 2005. Large mass
820 movements in relation to deglaciation in the Pyrenees: Proc. 6th Int. Conf. Geomor., Field Trip
821 Guide B-5, Zaragoza, Spain, 17 p.
822

823 García-Ruiz, J.M., Moreno, A., González-Sampérez, Valero-Garcés, B.L., Martí-Bono, C. 2010.
824 La cronología del último ciclo glacial en las montañas del sur de Europa: una revisión.
825 Cuaternario y Geomorfología 24: 35-46
826

827 García-Ruiz, J.M., Martí-Bono, C., Peña-Monne, J.L., Sancho, C., Rhodes, E.J., Valero-Garcés,
828 B., González-Sampérez, P., Moreno, A..2013. Glacial and fluvial deposits in the Aragón Valley,
829 central-western Pyrenees: chronology of the Pyrenean late Pleistocene glaciers. Geografiska
830 Annaler: Series A, Physical Geography, 95, 15–32.
831

832 Gori, S., Falucci, E., Dramis, F., Galadini, F., Galli, P., Giaccio, B., Messina, P., Pizzi, A.,
833 Sposato, A., Cosentino, D., 2014. Deep-seated gravitational slope deformation, large-scale rock
834 failure, and active normal faulting along Mt. Morrone (Sulmona basin, Central
835 Italy). Geomorphological and paleoseismological analyses: Geomorphology 208, 88-101.
836

837 Gutierrez, F., Acosta, E., Rios, S., Guerrero, J., Lucha, P., 2005. Geomorphology and
838 geochronology of sackung features (uphill-facing scarps) in the Central Spanish Pyrenees:
839 Geomorphology 69, 298-314.
840

841 Gutierrez, F., Ortuno, M., Lucha, P., Guerrero, J., Acosta, E., Coratza, P., Piacentini, D., Soldati,
842 M., 2008. Late Quaternary episodic displacement on a sackung scarp in the central Spanish
843 Pyrenees; Secondary paleoseismic evidence?: Geodin. Acta 21, 187-202.
844

845 Handwerker, A.L., Rempel, A.W., Skarbek, R.M., Roering, J.J., Hilley, G.E., 2016. Rate-
846 weakening friction characterizes both slow sliding and catastrophic failure of landslides. Proc.
847 Nat. Acad. Sci., Earth, Atmos., and Plan. Sci. 113, 10281-10286.
848

849 Hartevelt, J.J.A., 1970. Geology of the Upper Segre and Valira valleys, Central Pyrenees,
850 Andorra/Spain: Leidse Geolog. Mededelingen. 45, 167– 236.
851

852 Hippolyte, J.-C., Brocard, G., Tardy, M., Nicoud, G., Bourles, D., Braucher, R., Menard,
853 G., Souffache, B., 2006. The recent fault scarps of the Western Alps (France): Tectonic surface
854 ruptures or gravitational sackung scarps? A combined mapping, geomorphic, levelling, and ¹⁰Be
855 dating approach. Tectonophys. 418, 255–276.
856

857 Hippolyte, J.-C., Bourlès, D., Braucher, R., Carcaillet, J., Léanni, L., Arnold, M., Aumaitre, G.,
858 2009. Cosmogenic ¹⁰Be dating of a sackung and its faulted rock glaciers, in the Alps of Savoy
859 (France): Geomorphology 108, 312–320.
860

861 Huntley, D.J., Wintle, A.G., 1981. The use of alpha scintillation counting for measuring ²³⁰Th and
862 ²³¹Pa contents of ocean sediments. Canadian J. Earth Sci. 18, 419-432.
863

864 Hurlimann, M., Ledesma, A., Corominas, J., Prat, P.C., 2006. The deep-seated slope
865 deformation at Encampadana, Andorra; Representation of morphologic features by numerical
866 modeling. Engr. Geol. 83, 343-357.
867

868 Jarman, D., Calvet, M., Corominas, J., Delmas, M., Gunnell, Y., 2014. Large-scale rock slope
869 failures in the eastern Pyrenees; identifying a sparse but significant population in paraglacial
870 and parafluvial contexts. *Geograf. Ann.* 96, 357-391.
871

872 McCalpin, J.P., 2003. Criteria for determining the seismic significance of sackungen and other
873 scarplike landforms in mountainous regions, in Hart, E.W. (ed.), *Ridge-Top Spreading in*
874 *California; Contributions toward understanding a significant seismic hazard.* Calif. Geol. Surv.
875 CD 2003-05, 2 CD-ROMs.
876

877 McCalpin, J.P., 2005. Late Quaternary activity of the Pajarito fault, Rio Grande rift of northern
878 New Mexico, USA. *Tectonophys* 408, 213-236.
879

880 McCalpin J.P., 2013. Trenching and Exposed Faces, in Shroder, J.F., Switzer, A.D., Kennedy,
881 D.M. (Eds.) *Treatise on Geomorphology*, Vol. 14, *Methods in Geomorphology*: Academic Press,
882 San Diego, CA, 138-149.
883

884 McCalpin, J.P., Bruhn, R.L., Pavlis, T.L., Gutierrez, F., Guerrero, J., Lucha, P., 2011, Antislope
885 scarps, gravitational spreading, and tectonic faulting in the western Yakutat microplate, south
886 coastal Alaska. *Geosphere* 7, 1143-1158.
887

888 McCalpin, J.P., Hart, E.W., 2003. Ridge-top spreading features and relationship to earthquakes,
889 San Gabriel Mountains Region, Southern California - Part A: Distribution and description of
890 ridge-top depressions (sackungen), in Hart, E.W. (ed.), *Ridge-Top Spreading in California;*
891 *Contributions toward understanding a significant seismic hazard.* Calif. Geol. Surv. CD 2003-05,
892 2 CD-ROMs.
893

894 McCalpin, J.P., Hart, E.W., 2003. Ridge-top spreading features and relationship to earthquakes,
895 San Gabriel Mountains Region, Southern California - Part B: Paleoseismic investigations of
896 ridge-top depressions, in Hart, E.W. (ed.), *Ridge-Top Spreading in California; Contributions*
897 *toward understanding a significant seismic hazard.* Calif. Geol. Surv. CD 2003-05, 2 CD-ROMs.
898

899 McCalpin, J.P., Irvine, J.R., 1995. Sackungen at Aspen Highlands Ski Area, Pitkin County,
900 Colorado. *Environ. Engr. Geosci.* 1, 277-290.
901

902 Mariotto, F.P., Tibaldi, A., 2016. Inversion kinematics at deep-seated gravity slope deformations
903 revealed by trenching techniques. *Nat. Haz. Earth Syst. Sci.* 16, 663-674.
904

905 Olley, J.M., Murray, A., Roberts, R., 1996. The effects of disequilibria in the uranium and
906 thorium decay chains on burial dose rates in fluvial sediments. *Quat. Sci. Rev.* 15, 751-760.
907

908 Ortuño, M., Guinau, M., Calvet, J., Furdada, G., Bordonau, J., Ruiz, A., Camafort, M., 2017.
909 Potential of airborne LiDAR data analysis to detect subtle landforms of slope failure; Portainé,
910 Central Pyrenees. *Geomorphology* 295, 364-382.
911

912 Panek, T., Klimes, J., 2016. Temporal behavior of deep-seated gravitational slope deformations:
913 A review. *Earth. Sci. Rev.* 156, 14-38.
914

915 Panek, T., Mentlik, P., Ditchburn, B., Zondervan, A., Norton, K., Hradecky, J., 2015. Are
916 sackungen diagnostic features of (de)glaciated mountains? *Geomorphology* 248, 396-410.
917

918 Panek, T., Mentlik, P., Engel, Z., Braucher, R., Zondervan, A., The Aster Team, 2017. Late
919 Quaternary sackungen in the highest mountains of the Carpathians: *Quat. Sci. Rev.* 159, 47-62.
920

921 Reimer, P.J. and 27 others, 2013, IntCal13 and MARINE13 radiocarbon age calibration curves
922 0-50000 years cal BP. *Radiocarbon* 55, DOI: 10.2458/azu_js_rc.55.16947.
923

924 Soeters, R., Rengers, N. 1983. Dos ejemplos de hundimientos gravitacionales en los
925 alrededores de Caldes de Boí (Pirineos leridanos). In: *Geología de España- Libro Jubilar de*
926 *J.Mª Ríos. IGME. Madrid Vol.3: 193-202*
927

928 Soil Survey Staff, 2014. *Keys to Soil Taxonomy*, 12th ed. U.S. Dept. Agriculture, Natural
929 Resources Conservation Service, Washington, DC., USA, 360 p.
930

931 Soutadé, G. 1988. Le glissement d'el Forn (Andorra). II Simposio Inestabilidad de Taludes y
932 Laderas Naturales. Andorra la Vella. pp 643-655
933

934 Turu, V., 2002. Analisis secuencial del delta de Erts, estratigrafia de un valle glaciar obturado
935 intermitentemente; Relacion con enultimo ciclo glaciar., Valle de Arinsal, Pirineos Orientales. In:
936 *Estudios recientes (2000–2002) en geomorfología, patrimonio, montana y dinamica territorial.*
937 *SEG–Departamento de geografía UVA edit, Valladolid, 555–574.*
938

939 Turu, V. 2011. El glacialisme de les valls de la Valira del Nord: evidències d'un englaçament
940 continuat fins a l'Holocè. Resúmenes XIII Reunión Nacional de Cuaternario. Andorra. 6 pp.
941

942 Turu, V., Calvet, M., Bordenau, J., Gunnell, Y., Delmas, M., Vilaplana, J.M., Jalut, G., 2016, Did
943 Pyrenean glaciers dance to the beat of global climatic events? Evidence from the Würmian
944 sequence stratigraphy of an ice-dammed paleolake depocentre in Andorra, *in* Hughes, P.D. and
945 Woodward, J.C. (eds.), *Quaternary Glaciation in the Mediterranean Mountains.* Geol. Soc.
946 London Spec. Pub. 433, 111-136.
947

948 Wintle, A.G., Huntley, D.J., 1980. Thermoluminescence dating of ocean sediments: *Canadian J.*
949 *Earth Sci.* 17, 348-360.
950

951 Zwart, H.J. 1979. The geology of the Central Pyrenees. *Leidse Geologische Mededelingen*, 50:
952 1-74